A. De Vittori, M.F. Palermo, P. Di Lizia, R. Armellin
Low-Thrust Collision Avoidance Maneuver Optimization
Journal of Guidance Control and Dynamics, Vol. 45, N. 10, 2022, p. 1815-1829
doi:10.2514/1.G006630

Low-Thrust Collision Avoidance Maneuver Optimization

Andrea De Vittori,* Maria Francesca Palermo,† and Pierluigi Di Lizia‡
Polytechnic University of Milan, 20156 Milan, Italy
and
Roberto Armellin§
The University of Auckland, Auckland 1010, New Zealand

This work presents robust and numerically efficient algorithms for designing low-thrust collision avoidance maneuvers in short-term encounters. The conjunction dynamics are developed in a tridimensional space and then projected onto the B-plane, centered at the secondary object. Energy- and fuel-optimal maneuvers are computed by constraining the collision probability or the miss distance. A fully analytical approach is derived for energy-optimal collision avoidance maneuvers, providing a good guess for the fuel-optimal problem. The proposed methods are validated in terms of efficiency and robustness in a simulated scenario accounting for environmental perturbations.

I. Introduction

THE design of efficient collision avoidance maneuvers (CAMs) has a twofold objective: to enable autonomous spacecraft operations and to limit the growth of space debris. Generally in the low-Earth-orbit regime, hundreds of collision warnings are weekly issued. For the most, the risk drops as time goes on thanks to more refined orbit data. Whenever the probability of collision (P_c) or miss distance (d) exceeds a certain threshold at the time of closest approach (TCA), a CAM is performed. As the number of in-orbit satellites is growing day by day, the on-ground procedures presently used for CAM design and execution may suffer bottlenecks in the next future.

To optimize a CAM, a cost function (usually the total ΔV) is minimized enforcing some boundary constraints, such as the collision probability with one or more space objects. The existing state-of-the-art for continuous-thrust CAM optimization is limited. Research on this field includes semi-analytical techniques featured by Reiter and Spencer [1] for rapid CAM, with the assumption of optimal radial thrust. Although being analytical, the formulation only holds close to conjunction. Salemme et al. [2] described an indirect energy-optimal control problem (EOCP) and a fuel-optimal control problem (FOCP) in Cartesian coordinates with a prescribed P_c. Schiavo [3] continued in the same vein with semi-analytical and analytical computationally efficient methods for EOCP by imposing P_c as a boundary condition. In both [2] and [3] the routine requires an iterative process to satisfy boundary conditions; thus, it may not be suitable for an onboard implementation. Gonzalo et al. [4] proposed a semi-analytical approach mainly to maximize the miss distance with averaged equations of motion and a constant tangential thrust assumption. Recently, Hernando-Ayuso and Bombardelli [5] have proposed a solution for optimum low-thrust CAM design in B-plane coordinates for two resident space objects (RSOs) belonging to circular orbits. Just the thrust orientation is optimized (with constant magnitude) for a specified time window. While the B-plane reference frame (r.f.) lowers the resulting two-point boundary value problem (TPBVP) dimension from six to only two, the circular assumption and the rigid control structure are the two main limitations. The paper by Belmonte Hernandez et al. [6] illustrates two ways to design a low-thrust CAM: the first adopts a fuel-optimal transformation from the energy-optimal solution, and the latter addresses CAM with convex optimization. Likewise, Armellin [7] has devised a multi-impulse convex CAM optimization with both low-thrust and impulsive propulsion systems. Being a direct formulation, the chosen control parameterization can affect the solution's optimality.

This work proposes novel approaches based on indirect trajectory optimization for low-thrust CAM design, aiming at onboard implementation. The contribution is twofold. First, by leveraging previous results that demonstrated CAM dynamics to be almost linear [5,7], we develop a fully analytical solution for the energy-optimal problem without any assumptions on the RSO orbits or thrust direction. As a result, both formulations in Earth-centered inertial (ECI) and B-plane coordinates for unconstrained or tangential CAMs converge and achieve excellent computational efficiency. Secondly, these solutions provide accurate guesses for FOCPs enabling bounded thrust and reduced propellant consumption.

The paper is structured as follows. Firstly, Sec. II introduces the main mathematical concepts instrumental to framing the proposed methods. Next, Sec. III covers the derivation of low-thrust CAM with dynamics formulation in both ECI and BP reference frames. To fulfill constraints on the thrust profile, the EOCP provides the first guess for a fuel-optimal solution. Purely tangential maneuvers are also studied. Section IV analyzes the achieved algorithm time performance. Finally, conclusions are in Sec. V.

II. Mathematical Models

This section deals with the fundamentals of CAM design. Specifically, it details the basic principles of conjunction dynamics in the B-plane r.f., and then it provides a brief introduction to the selected P_c model.

A. B-Plane Definition

Let us focus on a conjunction event between two objects with relative closest approach position $\boldsymbol{r}_e$. Usually, the maneuverable object is defined as "primary," identified by the symbol O_p. The other uncooperative object is instead called "secondary" and labeled with O_s. The related state vectors are $\boldsymbol{x}_p = (\boldsymbol{r}_p, \boldsymbol{v}_p)$ and $\boldsymbol{x}_s = (\boldsymbol{r}_s, \boldsymbol{v}_s)$; $\boldsymbol{r}$ and $\boldsymbol{v}$ (with the corresponding subscripts p and s) are the center-of-mass position and velocity vectors of the two objects, generally set in an arbitrary r.f. $\hat{\Re}$.

The inertial r.f. centered at O_s is described by $\{x, y, z\}$ at TCA, with axes directions identified by

Received 13 December 2021; revision received 15 May 2022; accepted for publication 21 May 2022; published online 29 July 2022.

*Ph.D. Candidate, Department of Aerospace Science and Technology, Via La Masa 34; andrea.devittori@polimi.it.

†Graduate Student, Department of Aerospace Science and Technology, Via La Masa 34; mariafrancesca.palermo@mail.polimi.it.

‡Associate Professor, Department of Aerospace Science and Technology, Via La Masa 34; pierluigi.dilizia@polimi.it. Member AIAA.

§Professor, Te Pūnaha Ātea—Space Institute, 20 Symonds street, Auckland Central, Auckland 1010, New Zealand; roberto.armellin@auckland.ac.nz. Member AIAA.

$$\boldsymbol{u}_x = \frac{\boldsymbol{v}_p}{\|\boldsymbol{v}_p\|}, \qquad \boldsymbol{u}_z = \frac{\boldsymbol{v}_p \times \boldsymbol{v}_s}{\|\boldsymbol{v}_p \times \boldsymbol{v}_s\|}, \qquad \boldsymbol{u}_y = \boldsymbol{u}_z \times \boldsymbol{u}_x \tag{1}$$

The encounter duration t_c is defined as

$$t_c = \frac{2\sigma_\eta}{\|v_p - v_s\|} \tag{2}$$

where σ_η is the covariance in the η-axis direction specified hereafter in B-plane coordinates, v_p and v_s are instead the magnitudes of the velocity of the primary and secondary object, respectively. Whenever

$$\epsilon = \frac{t_c}{T_p} \ll 1 \approx 10^{-3} \tag{3}$$

the conjunction is called short-term. With T_p being the primary orbital period in Eq. (3), the involved objects motion approximates as uniform rectilinear (short-term encounter hypothesis; for further details, see [8]). The collision avoidance dynamics is pictured in the B-plane by adopting the formulation of [9]. This framework, depicted in Fig. 1, refers to the conjunction plane of two colliding space objects. It is oriented perpendicular to their relative velocity and embeds the primary and secondary at TCA. A useful coordinate system in this context is given by the position vector $\boldsymbol{b}_{3\mathrm{D}} = [\xi, \eta, \zeta]^\top$, framed in the B-plane as

$$\boldsymbol{u}_\xi = \frac{\boldsymbol{v}_s \times \boldsymbol{v}_p}{\|\boldsymbol{v}_s \times \boldsymbol{v}_p\|} \qquad \boldsymbol{u}_\eta = \frac{\boldsymbol{v}_p - \boldsymbol{v}_s}{\|\boldsymbol{v}_p - \boldsymbol{v}_s\|}, \qquad \boldsymbol{u}_\zeta = \boldsymbol{u}_\xi \times \boldsymbol{u}_\eta \tag{4}$$

The corresponding rotation matrix from the inertial r.f. to the B-plane reads

$$\boldsymbol{R}_{b,3\mathrm{D}} = [\boldsymbol{u}_\xi, \boldsymbol{u}_\eta, \boldsymbol{u}_\zeta]^\top \tag{5}$$

while the projection on the η axis is

$$\boldsymbol{R}_{b,2\mathrm{D}} = [\boldsymbol{u}_\xi, \boldsymbol{u}_\zeta]^\top \tag{6}$$

At TCA, primary orbital elements are stated as a_0 semimajor axis, e_0 eccentricity, R_c radial orbital distance, and θ_c true anomaly. To simplify the notation, the bidimensional B-plane position vector is written as $\boldsymbol{b} = [\xi, \zeta]^\top$, derived from the first and last components of $\boldsymbol{b}_{3\mathrm{D}}$.

The upcoming subsections give a quick recap on B-plane dynamics, focusing on the equations of motion for continuous low-thrust CAM.

B. Low-Thrust Collision Avoidance Dynamics

If the primary spacecraft O_p features a low-thrust propulsion system, the CAM design is assumed to optimally orient the thruster along the maneuver. The corresponding propelled dynamics in the ECI r.f. are

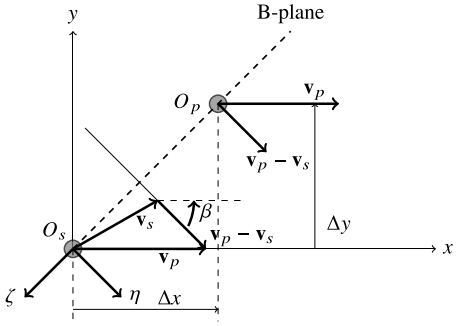

Fig. 1 Encounter frame and B-plane: snapshot of $O_p - O_s$ encounter geometry (x–y plane) after CAM.

$$\begin{cases} \dot{\boldsymbol{r}} = \boldsymbol{v} \\ \dot{\boldsymbol{v}} = -\frac{\mu}{r^3}\boldsymbol{r} + \boldsymbol{a}_c \end{cases} \qquad \text{ICs:} \begin{cases} \boldsymbol{r}(t_0) = \boldsymbol{r}_0 \\ \boldsymbol{v}(t_0) = \boldsymbol{v}_0 \end{cases} \tag{7}$$

where μ is the Earth gravitational parameter, $\boldsymbol{a}_c$ is the control acceleration, and t_0, $\boldsymbol{r}_0$, and $\boldsymbol{v}_0$ are the time and the spacecraft state at the CAM initial maneuvering point. "ICs" stands for initial conditions. No orbital perturbations are taken into account in the design phase (their effect is studied a posteriori on the designed CAM in Sec. IV.D), and the mass flow rate decouples from the dynamics:

$$\dot{m} = -\frac{1}{c_e}\|\boldsymbol{a}_c\| m \quad \text{IC}: m(t_0) = m_0 \tag{8}$$

where

$$c_e = I_{sp} g_0 \tag{9}$$

In Eq. (9), I_{sp} is the specific impulse and g_0 is the standard gravitational acceleration at ground level. Hernando-Ayuso and Bombardelli [5] suggest tackling the maneuver by analyzing the variation introduced on B-plane quantities. The infinitesimal velocity variation induced by the control acceleration $\boldsymbol{a}_c$ acting for an infinitesimal time δt is

$$\delta \boldsymbol{v} = \boldsymbol{a}_c \delta t \tag{10}$$

and it yields a B-plane displacement $\delta \boldsymbol{b} = [\delta\xi, \delta\zeta]^\top$:

$$\delta \boldsymbol{b} = \boldsymbol{R}\boldsymbol{K}\boldsymbol{D}(t)\boldsymbol{a}_c \delta t = \boldsymbol{M}(t)\boldsymbol{a}_c \delta t \tag{11}$$

Where the matrices $\boldsymbol{R}$, $\boldsymbol{K}$, and $\boldsymbol{D}$ are declared in [5] and relate to the rotation, kinematics, and dynamics from the ECI r.f. to the B-plane. $\boldsymbol{M}$, the product of the three matrices, is a function of time, being $\boldsymbol{D}$ dependent on the initial maneuvering point. With a first-order approximation and suited initial conditions, Eq. (11) transforms into a system of differential equations:

$$\dot{\boldsymbol{b}} = \boldsymbol{M}(t)\boldsymbol{a}_c \quad \text{ICs}: \boldsymbol{b}(t_0) = \boldsymbol{b}_e = [\xi_e, \zeta_e]^\top \tag{12}$$

in which the subscript e indicates expected quantities. This formulation reduces the problem dimension from 6 to 2, which may ease the solution of OCPs, yet it is valid for circular orbits only. A more refined conjunction dynamics derivation in B-plane coordinates can be found in [5].

C. Probability of Collision and Square Mahalanobis Distance

There are different ways to compute a bidimensional collision probability P_c. A suitable approach for the problem at hand is the formulation suggested by Chan in [8] truncated at $m = 3$. P_c derives by the integration of a scaled isotropic Gaussian distribution function over an elliptical cross section. If the latter approximates as a circular cross section of equal area, the collision probability turns into a Rician integral evaluated with the following convergent series:

$$P_c(u, v) = e^{-\frac{v}{2}} \sum_{m=0}^{\infty} \frac{v^m}{2^m m!} \left[1 - e^{-\frac{u}{2}} \sum_{k=0}^{m} \frac{u^k}{2^k k!} \right] \tag{13}$$

where u is the ratio of the impact cross-sectional area to the area of the 1σ covariance ellipse in the B-plane:

$$u = \frac{s_A^2}{\sigma_\xi \sigma_\zeta \sqrt{1 - \rho_{\xi\zeta}^2}} \tag{14}$$

and v is the squared Mahalanobis distance d_M^2 :

$$v = d_M^2 = (\boldsymbol{r}_f - \boldsymbol{r}_s)^\top \boldsymbol{R}_{b,2\mathrm{D}}^\top \boldsymbol{C}^{-1} \boldsymbol{R}_{b,2\mathrm{D}} (\boldsymbol{r}_f - \boldsymbol{r}_s) = \boldsymbol{b}_f^\top \boldsymbol{C}^{-1} \boldsymbol{b}_f \tag{15}$$

$\boldsymbol{C}$ refers to the summed covariance matrix in B-plane axes of the two bodies, framed in the same orthonormal base (i.e., the two Gaussian

quantities are statistically independent) and then projected onto this reference system with components $\{\xi, \zeta\}$:

$$\boldsymbol{C} = \begin{bmatrix} \sigma_\xi^2 & \rho_{\xi\zeta}\sigma_\xi\sigma_\zeta \\ \rho_{\xi\zeta}\sigma_\xi\sigma_\zeta & \sigma_\zeta^2 \end{bmatrix} \tag{16}$$

The miss distance is just $d = \sqrt{\xi_e^2 + \zeta_e^2} = \|\boldsymbol{b}_f\| = \|\boldsymbol{R}_{b,2\mathrm{D}}(\boldsymbol{r}_f - \boldsymbol{r}_s)\|$.

III. Low-Thrust Collision Avoidance Maneuver Design

The mathematical derivations of the optimal low-thrust CAMs, in both ECI and B-plane r.f., are reported hereafter. The optimal control problems formulate using [10] as a primary reference.

A. Energy-Optimal CAM Design in ECI Coordinates

Let us delve into the controlled motion of the primary object around the Earth, considering the propelled Keplerian dynamics introduced in Eq. (7). In the EOCP, the control identifies with an acceleration vector $\boldsymbol{a}_c = [a_{c,x}, a_{c,y}, a_{c,z}]^\top$. For numerical reasons, it specifies as $\boldsymbol{a}_c = a_{\max}\epsilon\boldsymbol{\alpha}$, where $a_{\max}$ is a scaling parameter corresponding to the current spacecraft mass and maximum thrust, ϵ modulates $a_{\max}$, and $\boldsymbol{\alpha} = \boldsymbol{a}_c/a_c$ is the thrust direction.

In the EOCP the cost function is defined as

$$J = \int_{t_0}^{t_f} \frac{1}{2} a_{\max}\epsilon^2 \, \mathrm{d}t \tag{17}$$

and the terminal condition can be set in terms of squared Mahalanobis distance d_M^2 [or equivalently as P_c, by way of Eq. (13)] or miss distance d. These two conditions are treated separately in the following subsections.

1. *Square Mahalanobis Distance Constraint*

In this approach the primary relative position $\boldsymbol{r}_f = \boldsymbol{r}(t_f)$ at conjunction is enforced to match a predefined square Mahalanobis distance $\bar{d}_M^2$ value. The resulting terminal condition is

$$\Psi(\boldsymbol{x}(t_f), t_f) = d_M^2(\boldsymbol{r}_f) - \bar{d}_M^2 = 0 \tag{18}$$

The augmented cost function becomes

$$\overline{J} = \nu[d_M^2(\boldsymbol{r}_f) - \bar{d}_M^2] + \int_{t_0}^{t_f} \left\{ \frac{1}{2} a_{\max}\epsilon^2 + \boldsymbol{\lambda}^\top(t)[\dot{\boldsymbol{x}}(t) - \boldsymbol{f}(\boldsymbol{x}, \boldsymbol{a}_c)] \right\} \mathrm{d}t \tag{19}$$

Here $\boldsymbol{f}$ embeds the problem dynamics, $\dot{\boldsymbol{x}} = \boldsymbol{f}(\boldsymbol{x}, \boldsymbol{a}_c)$ given in Eq. (7), and ν is an additional Lagrangian multiplier paired with the terminal constraint. The resulting Hamiltonian is

$$H = \frac{1}{2} a_{\max}\epsilon^2 + \boldsymbol{\lambda}_r^\top \boldsymbol{v} + \boldsymbol{\lambda}_v^\top \left(-\frac{\mu}{r^3}\boldsymbol{r} + \epsilon a_{\max}\boldsymbol{\alpha} \right) \tag{20}$$

The optimal control law, expressed in terms of optimal $(\epsilon^*, \boldsymbol{\alpha}^*)$, i.e., the acceleration norm and unit vector, respectively, results from the Pontryagin's minimum principle.

$$\boldsymbol{\alpha}^* = -\boldsymbol{\lambda}_v/\lambda_v, \qquad \epsilon^* = \lambda_v \tag{21}$$

Hence, the optimal control acceleration $\boldsymbol{a}_c^* = a_{\max}\epsilon^*\boldsymbol{\alpha}^* = -a_{\max}\boldsymbol{\lambda}_v$. The term $a_{\max}$ scales the velocity costate to be one in magnitude when commanding the maximum available acceleration. Then, the Euler–Lagrange equations read:

$$\begin{cases} \dot{\boldsymbol{r}} = \boldsymbol{v} \\ \dot{\boldsymbol{v}} = -\frac{\mu}{r^3}\boldsymbol{r} - a_{\max}\boldsymbol{\lambda}_v \\ \dot{\boldsymbol{\lambda}}_r = \frac{\mu}{r^3}\boldsymbol{\lambda}_v - \frac{3\mu \boldsymbol{r}\cdot\boldsymbol{\lambda}_v}{r^5}\boldsymbol{r} \\ \dot{\boldsymbol{\lambda}}_v = -\boldsymbol{\lambda}_r, \end{cases}$$

$$BC: \begin{cases} \boldsymbol{r}(t_0) = \boldsymbol{r}_0 \\ \boldsymbol{v}(t_0) = \boldsymbol{v}_0 \\ \boldsymbol{\lambda}_r(t_f) = \nu \frac{\partial d_M^2(\boldsymbol{r}_f)}{\partial \boldsymbol{r}_f} = 2\nu \boldsymbol{R}_{2\mathrm{D}}^\top \boldsymbol{C}^{-1} \boldsymbol{R}_{2\mathrm{D}}(\boldsymbol{r}_f - \boldsymbol{r}_s) \\ \boldsymbol{\lambda}_v(t_f) = \nu \frac{\partial d^2(\boldsymbol{v}_f)}{\partial \boldsymbol{v}_f} = \boldsymbol{0} \\ d_M^2(\boldsymbol{r}_f) - \bar{d}_M^2 = 0 \end{cases} \tag{22}$$

Equation (22) forms a TPBVP, usually solved iteratively with computationally expensive methods; the convergence is highly affected by the first guess solution. Here the TPBVP is addressed analytically by linearizing the motion of Eq. (22) about the nominal uncontrolled dynamics. The aim is to pinpoint the initial costates $\boldsymbol{\lambda}_{r0}$, $\boldsymbol{\lambda}_{v0}$ as to reduce the TPBVP to an initial value problem (IVP) employing the terminal constraint and the STM determined through the integration of the following dynamics:

$$\dot{\boldsymbol{\Phi}}(t, t_0) = \boldsymbol{A}(t)\boldsymbol{\Phi}(t, t_0), \quad \boldsymbol{\Phi}(t_0, t_0) = \mathbb{I}_{n\times n} \tag{23}$$

where $\boldsymbol{A}$ is the Jacobian of the dynamics in Eq. (22) evaluated on a purely Keplerian motion.

$$\boldsymbol{A} = \begin{bmatrix} \boldsymbol{0}_{3\times3} & \mathbb{I}_{3\times3} & \boldsymbol{0}_{3\times3} & \boldsymbol{0}_{3\times3} \\ -\boldsymbol{A}_{34} & \boldsymbol{0}_{3\times3} & \boldsymbol{0}_{3\times3} & -a_{\max}\mathbb{I}_{3\times3} \\ \boldsymbol{0}_{3\times3} & \boldsymbol{0}_{3\times3} & \boldsymbol{0}_{3\times3} & \boldsymbol{A}_{34} \\ \boldsymbol{0}_{3\times3} & \boldsymbol{0}_{3\times3} & -\mathbb{I}_{3\times3} & \boldsymbol{0}_{3\times3} \end{bmatrix},$$

$$\text{with } \boldsymbol{A}_{34} = \frac{\mu}{r^3}\mathbb{I}_{3\times3} - 3\frac{\mu}{r^5}\overbrace{\begin{bmatrix} r_x\boldsymbol{r} & r_y\boldsymbol{r} & r_z\boldsymbol{r} \end{bmatrix}}^{3\times3 \text{ matrix}} \tag{24}$$

where r_x, r_y, and r_z refer to the position vector components. In $\boldsymbol{A}_{34}$, $\boldsymbol{r}$ is a column vector horizontally stacked to form 3 by 3 matrices. Next, the STM maps initial state variations into the corresponding final ones:

$$\begin{bmatrix} \delta\boldsymbol{r}_f \\ \delta\boldsymbol{v}_f \\ \delta\boldsymbol{\lambda}_{rf} \\ \delta\boldsymbol{\lambda}_{vf} \end{bmatrix} = \begin{bmatrix} \boldsymbol{\Phi}_{11} & \boldsymbol{\Phi}_{12} & \boldsymbol{\Phi}_{13} & \boldsymbol{\Phi}_{14} \\ \boldsymbol{\Phi}_{21} & \boldsymbol{\Phi}_{22} & \boldsymbol{\Phi}_{23} & \boldsymbol{\Phi}_{24} \\ \boldsymbol{\Phi}_{31} & \boldsymbol{\Phi}_{32} & \boldsymbol{\Phi}_{33} & \boldsymbol{\Phi}_{34} \\ \boldsymbol{\Phi}_{41} & \boldsymbol{\Phi}_{42} & \boldsymbol{\Phi}_{43} & \boldsymbol{\Phi}_{44} \end{bmatrix} \begin{bmatrix} \delta\boldsymbol{r}_0 \\ \delta\boldsymbol{v}_0 \\ \delta\boldsymbol{\lambda}_{r0} \\ \delta\boldsymbol{\lambda}_{v0} \end{bmatrix} \tag{25}$$

Provided an initial fixed state, $\delta\boldsymbol{r}_0 = \boldsymbol{0}$ and $\delta\boldsymbol{v}_0 = \boldsymbol{0}$. Moreover, the costates are set to zero on the nominal trajectory, i.e., $\delta\boldsymbol{\lambda}_{r0} = \boldsymbol{\lambda}_{r0}, \delta\boldsymbol{\lambda}_{v0} = \boldsymbol{\lambda}_{v0}, \delta\boldsymbol{\lambda}_{rf} = \boldsymbol{\lambda}_{rf}, \delta\boldsymbol{\lambda}_{vf} = \boldsymbol{\lambda}_{vf}$. The state variations at TCA are $\delta\boldsymbol{r}_f = \boldsymbol{r}_f - \boldsymbol{r}_p, \delta\boldsymbol{v}_f = \boldsymbol{v}_f - \boldsymbol{v}_p$. Equation (25) can be manipulated to find the initial costates $\boldsymbol{\lambda}_{r0}, \boldsymbol{\lambda}_{v0}$ as functions of the position $\boldsymbol{r}_f$ at conjunction. Considering that the final velocity is unconstrained, the corresponding costate is null: $\delta\boldsymbol{\lambda}_{vf} = \boldsymbol{\lambda}_{vf} = \boldsymbol{0}$. Therefore, from the fourth row of Eq. (25) and the third row of Eq. (25), the following can be derived:

$$\boldsymbol{\lambda}_{v0} = -\boldsymbol{\Phi}_{44}^{-1}\boldsymbol{\Phi}_{43}\delta\boldsymbol{\lambda}_{r0}, \quad \boldsymbol{\lambda}_{r0} = \boldsymbol{B}^{-1}\delta\boldsymbol{\lambda}_{rf},$$
$$\text{with } \boldsymbol{B} = \boldsymbol{\Phi}_{33} - \boldsymbol{\Phi}_{34}\boldsymbol{\Phi}_{44}^{-1}\boldsymbol{\Phi}_{43} \tag{26}$$

From the first row of Eq. (25),

$$\delta \boldsymbol{r}_f = \boldsymbol{D}\boldsymbol{B}^{-1}\delta\boldsymbol{\lambda}_{rf} \quad \text{, with } \boldsymbol{D} = \boldsymbol{\Phi}_{13} - \boldsymbol{\Phi}_{14}\boldsymbol{\Phi}_{44}^{-1}\boldsymbol{\Phi}_{43} \tag{27}$$

Since $\delta\boldsymbol{\lambda}_{rf} = \boldsymbol{\lambda}_{rf}$, Eq. (27) reads

$$\delta \boldsymbol{r}_f = \boldsymbol{D}\boldsymbol{B}^{-1}\boldsymbol{\lambda}_{rf} = \boldsymbol{D}\boldsymbol{B}^{-1}\nu\frac{\partial d_M^2(\boldsymbol{r}_f)}{\partial \boldsymbol{r}_f} = 2\nu\boldsymbol{D}\boldsymbol{B}^{-1}\boldsymbol{R}_{2\mathrm{D}}^{\top}\boldsymbol{C}^{-1}\boldsymbol{R}_{2\mathrm{D}}(\boldsymbol{r}_f - \boldsymbol{r}_s) \tag{28}$$

Overall, Eq. (28) and the last boundary condition on the SMD of Eq. (22) form a nonlinear system in $\boldsymbol{r}_f$ and ν. The first row is multiplied to the left by $\boldsymbol{R}_{2\mathrm{D}}$, and the second equation is reframed using the final position $\boldsymbol{b}_f$ in the B-plane:

$$\begin{cases} \boldsymbol{r}_f - \boldsymbol{r}_p = 2\nu\boldsymbol{D}\boldsymbol{B}^{-1}\boldsymbol{R}_{2\mathrm{D}}^{\top}\boldsymbol{C}^{-1}\boldsymbol{R}_{2\mathrm{D}}(\boldsymbol{r}_f - \boldsymbol{r}_s) \\ (\boldsymbol{r}_f - \boldsymbol{r}_s)^{\top}\boldsymbol{R}_{2\mathrm{D}}^{\top}\boldsymbol{C}^{-1}\boldsymbol{R}_{2\mathrm{D}}(\boldsymbol{r}_f - \boldsymbol{r}_s) = \bar{d}_M^2. \end{cases}$$
$$\Rightarrow \begin{cases} \boldsymbol{R}_{2\mathrm{D}}(\boldsymbol{r}_f - \boldsymbol{r}_p) = 2\nu\boldsymbol{R}_{2\mathrm{D}}\boldsymbol{D}\boldsymbol{B}^{-1}\boldsymbol{R}_{2\mathrm{D}}^{\top}\boldsymbol{C}^{-1}\boldsymbol{R}_{2\mathrm{D}}(\boldsymbol{r}_f - \boldsymbol{r}_s) \\ \boldsymbol{b}_f^{\top}\boldsymbol{C}^{-1}\boldsymbol{b}_f = \bar{d}_M^2 \end{cases} \tag{29}$$

Focusing on the first equation of Eq. (29), since a generic position $\boldsymbol{b}$ in the B-plane r.f. can be expressed as $\boldsymbol{b} = \boldsymbol{R}_{2\mathrm{D}}(\boldsymbol{r} - \boldsymbol{r}_s)$, we have

$$\boldsymbol{R}_{2\mathrm{D}}(\boldsymbol{r}_f - \boldsymbol{r}_s - \boldsymbol{r}_p + \boldsymbol{r}_s) = 2\nu\boldsymbol{R}_{2\mathrm{D}}\boldsymbol{D}\boldsymbol{B}^{-1}\boldsymbol{R}_{2\mathrm{D}}^{\top}\boldsymbol{C}^{-1}\boldsymbol{R}_{2\mathrm{D}}(\boldsymbol{r}_f - \boldsymbol{r}_s) \Rightarrow \boldsymbol{b}_f - \boldsymbol{b}_p = 2\nu\boldsymbol{R}_{2\mathrm{D}}\boldsymbol{D}\boldsymbol{B}^{-1}\boldsymbol{R}_{2\mathrm{D}}^{\top}\boldsymbol{C}^{-1}\boldsymbol{b}_f \tag{30}$$

By defining the matrix $\boldsymbol{E} = 2\boldsymbol{R}_{2\mathrm{D}}\boldsymbol{D}\boldsymbol{B}^{-1}\boldsymbol{R}_{2\mathrm{D}}^{\top}\boldsymbol{C}^{-1}$, Eq. (30) becomes

$$\boldsymbol{b}_f = (\mathbb{I}_{2\times 2} - \nu\boldsymbol{E})^{-1}\boldsymbol{b}_p \tag{31}$$

Replacing Eq. (31) in the second equation of Eq. (29), the latter leads to a scalar equation with unknown variable ν. More specifically,

$$[(\mathbb{I}_{2\times 2} - \nu\boldsymbol{E})^{-1}\boldsymbol{b}_p]^{\top}\boldsymbol{C}^{-1}(\mathbb{I}_{2\times 2} - \nu\boldsymbol{E})^{-1}\boldsymbol{b}_p = \bar{d}_M^2 \tag{32}$$

Since

$$(\mathbb{I} - \nu\boldsymbol{E})^{-1} = \frac{1}{\det(\mathbb{I} - \nu\boldsymbol{E})}[\mathbb{I} - \nu\ \det\boldsymbol{E}\cdot(\boldsymbol{E})^{-1}] \tag{33}$$

By setting $\tilde{\boldsymbol{E}} = \det\boldsymbol{E}\cdot\boldsymbol{E}^{-1}$ to streamline the notation, Eq. (32) can be manipulated and solved in closed-form for ν:

$$\nu^2(\tilde{\boldsymbol{E}}\boldsymbol{b}_p)^{\top}\boldsymbol{C}^{-1}(\tilde{\boldsymbol{E}}\boldsymbol{b}_p) - \nu[\boldsymbol{b}_p^{\top}\boldsymbol{C}^{-1}\tilde{\boldsymbol{E}}\boldsymbol{b}_p + (\tilde{\boldsymbol{E}}\boldsymbol{b}_p)^{\top}\boldsymbol{C}^{-1}\boldsymbol{b}_p] = \bar{d}_M^2\det^2(\mathbb{I} - \nu\boldsymbol{E}) - \boldsymbol{b}_p^{\top}\boldsymbol{C}^{-1}\boldsymbol{b}_p \tag{34}$$

Equation (34) has four solutions because the term with the quadratic determinant contains ν at the fourth degree. Depending on the polynomial coefficients, if all roots are real the solutions will be two local minima and two local maxima of the cost function J (as shown in the results section by Fig. 7). Through the already computed state transition matrix (STM), the linearized costates are easily retrieved, plugged into the acceleration definition and integrated over time to assess the Δv. The minimum across all solutions is selected, and the linked initial costates serve for the nonlinear controlled dynamics propagation.

The associated final position $\boldsymbol{r}_f$ reached after CAM execution can be found by inserting ν into the first equation of Eq. (29). Once $\boldsymbol{r}_f$ and ν are known, recalling that $\delta\boldsymbol{r}_f = \boldsymbol{r}_f - \boldsymbol{r}_p$, the initial costates $\boldsymbol{\lambda}_{r0}$ and $\boldsymbol{\lambda}_{v0}$ are finally computed from Eqs. (26) and (27):

$$\boldsymbol{\lambda}_{r0} = 2\nu\boldsymbol{B}^{-1}\boldsymbol{R}_{2\mathrm{D}}^{\top}\boldsymbol{C}^{-1}\boldsymbol{R}_{2\mathrm{D}}[-(\mathbb{I} - 2\nu\boldsymbol{D}\boldsymbol{B}^{-1}\boldsymbol{R}_{2\mathrm{D}}^{\top}\boldsymbol{C}^{-1}\boldsymbol{R}_{2\mathrm{D}})^{-1}(\boldsymbol{r}_p - \boldsymbol{r}_s) - \boldsymbol{r}_s] \tag{35}$$

$$\boldsymbol{\lambda}_{v0} = -2\nu\boldsymbol{\Phi}_{44}^{-1}\boldsymbol{\Phi}_{43}\boldsymbol{B}^{-1}\boldsymbol{R}_{2\mathrm{D}}^{\top}\boldsymbol{C}^{-1}\boldsymbol{R}_{2\mathrm{D}}[-(\mathbb{I} - 2\nu\boldsymbol{D}\boldsymbol{B}^{-1}\boldsymbol{R}_{2\mathrm{D}}^{\top}\boldsymbol{C}^{-1}\boldsymbol{R}_{2\mathrm{D}})^{-1}(\boldsymbol{r}_p - \boldsymbol{r}_s) - \boldsymbol{r}_s] \tag{36}$$

Thanks to the costates at t_0, the solution of the optimal control problem reduces to an IVP; i.e., the control laws of the optimal CAM are computed by integrating the nonlinear dynamics of Eq. (22). These are provided in Eqs. (35) and (36) through the motion linearization supplied by the STM. The whole method presented so far is summarized in Algorithm 1 for a set of arbitrary starting maneuvering points.

2. Miss Distance Constraint

The EOCP maneuver can be reformulated to set a constraint on the miss distance d. The miss distance d can be written as $d = \sqrt{\xi_e^2 + \zeta_e^2} = \|\boldsymbol{b}_f\| = \|\boldsymbol{R}_{2\mathrm{D}}(\boldsymbol{r}_f - \boldsymbol{r}_s)\|$. The nonlinear system in Eq. (29) becomes

Algorithm 1: EOCP-ECI

Input: CDM, $\overline{d_M^2} or \overline{P_c}, \bar{d}, \Delta\theta_{range}$
Output: $\boldsymbol{r}_f$, d_M^2 and P_c or d, $\boldsymbol{a}_c$, $\Delta\boldsymbol{v}$, Δm
Algorithm:
if $\overline{P_c}$ **then**
  $\overline{d_M^2} = P_c\_2\_squared\_mahalanobis\_distance(\overline{P_c})$
end if
Select a $\Delta\theta$
Start up true anomaly for maneuvering:
$\theta_m = \theta_{\mathrm{TCA}} - \Delta\theta$
T interval of time corresponding to $\Delta\theta$
span_backward = [T 0]
tspan_forward = [0 T]
Backward propagation:
Propagate the dynamics backward from θ_{TCA} to θ_m with a pure ballistic motion.
$[\boldsymbol{r}_0, \boldsymbol{v}_0] = keplerian\_propagation([\boldsymbol{r}_{\mathrm{TCA}}, \boldsymbol{v}_{\mathrm{TCA}}]$, tspan_backward, $\mu)$
Compute STM:
Starting from $[\boldsymbol{r}_0, \boldsymbol{v}_0]$, propagate the dynamics with keplerian_propagation alongside the STM for tspan_forward
Solve the nonlinear system:
if d_M^2 **then**
  Solve [Eq. (34)] for ν and compute $\boldsymbol{\lambda}_{r0}, \boldsymbol{\lambda}_{v0}$ in [Eqs. (35) and (36)]
Else
  Solve [Eq. (40)] for ν and compute $\boldsymbol{\lambda}_{r0}, \boldsymbol{\lambda}_{v0}$ in [Eqs. (41) and (42)]
end if
Controlled forward propagation:
$[\boldsymbol{R}, \boldsymbol{V}, \boldsymbol{\Lambda}_r, \boldsymbol{\Lambda}_v, \boldsymbol{m}] = control\_propagation([\boldsymbol{r}_0, \boldsymbol{v}_0, \boldsymbol{\lambda}_{r0}, \boldsymbol{\lambda}_{v0}, m_0]$, tspan_forward, $a_{max}, \mu)$ using the dynamics of Eq. (22) or in Eq. (63) for the tangential case.
$\boldsymbol{R}, \boldsymbol{V}, \boldsymbol{\Lambda}_r, \boldsymbol{\Lambda}_v$ are, respectively, n by 3 state and costate matrices; $\boldsymbol{m}$ is the mass array of dimension n; n represents the number of integration steps.
Output computation:
$\boldsymbol{r}_f = \boldsymbol{R}(end, :)$
$m_f = \boldsymbol{m}(end)$ final mass
Acceleration profile $\boldsymbol{a}_c$ retrieved by plugging $[\boldsymbol{R}, \boldsymbol{V}, \boldsymbol{\Lambda}_r, \boldsymbol{\Lambda}_v]$ in Eq. (22) or in Eq. (63) for the tangential case.
$\Delta\boldsymbol{v}$ is calculated with the integration of $|\boldsymbol{a}_c|$ in time.
$\Delta\boldsymbol{r} = \boldsymbol{r}_f - \boldsymbol{r}_s$
if d_M^2 **then**
  $d_M^2 = squared\_mahalanobis\_distance(\Delta\boldsymbol{r}, \mathrm{CDM})$
  $P_c = P_c\_chan(\Delta\boldsymbol{r}, \mathrm{CDM})$
else
  $d = miss\_distance(\Delta\boldsymbol{r}, \mathrm{CDM})$
end if
$\Delta m = m_f - m_0$
$\Delta\boldsymbol{r}$ B-plane projection

$$\begin{cases} \delta \boldsymbol{r}_f = 2\nu \boldsymbol{D}\boldsymbol{B}^{-1}\boldsymbol{R}_{2\mathrm{D}}^{\top}\boldsymbol{R}_{2\mathrm{D}}(\boldsymbol{r}_f - \boldsymbol{r}_s) \\ d(\boldsymbol{r}_f) = \overline{d}, \end{cases} \Rightarrow \begin{cases} \boldsymbol{R}_{2\mathrm{D}}(\boldsymbol{r}_f - \boldsymbol{r}_p) = 2\nu \boldsymbol{R}_{2\mathrm{D}}\boldsymbol{D}\boldsymbol{B}^{-1}\boldsymbol{R}_{2\mathrm{D}}^{\top}\boldsymbol{R}_{2\mathrm{D}}(\boldsymbol{r}_f - \boldsymbol{r}_s) \\ \|\boldsymbol{R}_{2\mathrm{D}}(\boldsymbol{r}_f - \boldsymbol{r}_s)\| = \overline{d} \end{cases} \tag{37}$$

By applying a procedure similar to the one presented above [Eqs. (30) and (31)], the first equation of Eq. (37) reads

$$\boldsymbol{b}_f = (\mathbb{I}_{2\times 2} - \nu \boldsymbol{E})^{-1}\boldsymbol{b}_p, \quad \text{with } \boldsymbol{E} = 2\boldsymbol{R}_{2\mathrm{D}}\boldsymbol{D}\boldsymbol{B}^{-1}\boldsymbol{R}_{2\mathrm{D}}^{\top} \tag{38}$$

whereas the second equation of Eq. (37) becomes

$$\left\| \frac{1}{\det(\mathbb{I} - \nu \boldsymbol{E})}(\mathbb{I} - \nu \tilde{\boldsymbol{E}})\boldsymbol{b}_p \right\| = \overline{d} \tag{39}$$

and the final fourth order polynomial in ν transforms into

$$\nu^2(\tilde{\boldsymbol{E}}\boldsymbol{b}_p)^{\top}(\tilde{\boldsymbol{E}}\boldsymbol{b}_p) - \nu \boldsymbol{b}_p^{\top}\tilde{\boldsymbol{E}}\boldsymbol{b}_p - \nu(\tilde{\boldsymbol{E}}\boldsymbol{b}_p)^{\top}\boldsymbol{b}_p = \det(\mathbb{I} - \nu \boldsymbol{E})^2\overline{d}^2 - \boldsymbol{b}_p^{\top}\boldsymbol{b}_p \tag{40}$$

Similarly to the d_M^2, Eq. (40) is algebraically manipulated and analytically solved for ν to retrieve the initial costates $\boldsymbol{\lambda}_{r0}$ and $\boldsymbol{\lambda}_{v0}$:

$$\boldsymbol{\lambda}_{r0} = 2\nu \boldsymbol{B}^{-1}\boldsymbol{R}_{2\mathrm{D}}^{\top}\boldsymbol{R}_{2\mathrm{D}}[-(\mathbb{I} - 2\nu \boldsymbol{D}\boldsymbol{B}^{-1}\boldsymbol{R}_{2\mathrm{D}}^{\top}\boldsymbol{R}_{2\mathrm{D}})^{-1}(\boldsymbol{r}_p - \boldsymbol{r}_s) - \boldsymbol{r}_s] \tag{41}$$

$$\boldsymbol{\lambda}_{v0} = -2\nu \boldsymbol{\Phi}_{44}^{-1}\boldsymbol{\Phi}_{43}\boldsymbol{B}^{-1}\boldsymbol{R}_{2\mathrm{D}}^{\top}\boldsymbol{R}_{2\mathrm{D}}[-(\mathbb{I} - 2\nu \boldsymbol{D}\boldsymbol{B}^{-1}\boldsymbol{R}_{2\mathrm{D}}^{\top}\boldsymbol{R}_{2\mathrm{D}})^{-1} (\boldsymbol{r}_p - \boldsymbol{r}_s) - \boldsymbol{r}_s] \tag{42}$$

The solution of the optimal control problem turns into an IVP. The control laws of the optimal CAM are found by integrating the dynamics Eq. (22) starting from the nominal initial state and the costates given in Eqs. (41) and (42). As in the square Mahalanobis distance case, Algorithm 1 provides a quick recap on the miss distance problem implementation.

B. Energy-Optimal CAM Design in B-Plane Coordinates

The EOCP can be transposed in the B-plane to lower the system dimension. The state vector in the B-plane r.f. is $\boldsymbol{b} = [b_\xi, b_\zeta]^{\top}$. The controlled dynamics is

$$\begin{cases} \dot{\boldsymbol{b}} = a_{\max}\epsilon \boldsymbol{M}(t)\boldsymbol{\alpha} \\ \boldsymbol{b}(t_0) = \boldsymbol{b}_0 \end{cases}, \quad \text{with } \boldsymbol{M}(t) = \boldsymbol{R}\boldsymbol{K}\boldsymbol{D}(t) \tag{43}$$

The performance index is still expressed as in Eq. (17). Similarly to the Cartesian r.f., the terminal function can set a constraint on either d_M^2 (covering the case of a fixed P_c as well) or d.

1. *Squared Mahalanobis Distance Constraint*

The problem is here formulated to force the final d_M^2 to equal a fixed value $\bar{d}_M^2$. Hence, the Hamiltonian system of the EOCP is

$$\begin{cases} \dot{\boldsymbol{b}} = -a_{\max}\boldsymbol{M}(t)\boldsymbol{M}(t)^{\top}\boldsymbol{\lambda} \\ \dot{\boldsymbol{\lambda}} = \boldsymbol{0}. \end{cases} \quad BC: \begin{cases} \boldsymbol{b}(t_0) = \boldsymbol{b}_0 \\ \boldsymbol{\lambda}(t_f) = \dfrac{\partial d_M^2(\boldsymbol{b}_f)}{\partial \boldsymbol{b}_f} = 2\nu \boldsymbol{C}^{-1}\boldsymbol{b}(t_f) \\ \boldsymbol{b}^{\top}(t_f)\boldsymbol{C}^{-1}\boldsymbol{b}(t_f) - \bar{d}_M^2 = 0 \end{cases} \tag{44}$$

Since the problem does not explicitly depend on $\boldsymbol{b}$, $\boldsymbol{\lambda}$ is constant over time:

$$\boldsymbol{\lambda}(t_0) = \boldsymbol{\lambda}(t) = \nu 2\boldsymbol{C}^{-1}\boldsymbol{b}(t_f), \quad \forall\ t \in (t_0, t_f) \tag{45}$$

Equation (44) are linear. Thus, the exact solution of the above TPBVP can be obtained using the STM attained through the following dynamics:

$$\dot{\boldsymbol{\Phi}}(t, t_0) = \boldsymbol{A}(t)\boldsymbol{\Phi}(t, t_0), \quad \boldsymbol{\Phi}(t_0, t_0) = \mathbb{I}_{4\times 4} \tag{46}$$

where $\boldsymbol{A}(t)$ for this specific case reads

$$\boldsymbol{A} = \begin{bmatrix} \boldsymbol{0}_{2\times 2} & -a_{\max}\boldsymbol{M}(t)\boldsymbol{M}(t)^{\top} \\ \boldsymbol{0}_{2\times 2} & \boldsymbol{0}_{2\times 2} \end{bmatrix}, \quad \text{such that: } \begin{bmatrix} \dot{\boldsymbol{b}} \\ \dot{\boldsymbol{\lambda}} \end{bmatrix} = \boldsymbol{A}\begin{bmatrix} \boldsymbol{b} \\ \boldsymbol{\lambda} \end{bmatrix} \tag{47}$$

where $\boldsymbol{M}(t)$ corresponds to the uncontrolled motion.

The resulting STM links the initial state and costate to their final values as

$$\begin{bmatrix} \delta \boldsymbol{b}_f \\ \delta \boldsymbol{\lambda}_f \end{bmatrix} = \begin{bmatrix} \boldsymbol{\Phi}_{11} & \boldsymbol{\Phi}_{12} \\ \boldsymbol{\Phi}_{21} & \boldsymbol{\Phi}_{22} \end{bmatrix}\begin{bmatrix} \delta \boldsymbol{b}_0 \\ \delta \boldsymbol{\lambda}_0 \end{bmatrix} \tag{48}$$

Since the initial state is fixed, $\delta \boldsymbol{b}_0 = \boldsymbol{0}$. Moreover, the costate is null on the uncontrolled trajectory, i.e., $\delta \boldsymbol{\lambda}_0 = \boldsymbol{\lambda}_0$. Consequently, the state and costate variations at TCA after CAM execution are

$$\delta \boldsymbol{b}_f = \boldsymbol{b}_f - \boldsymbol{b}_e, \qquad \delta \boldsymbol{\lambda}_f = \boldsymbol{\lambda}_f \tag{49}$$

Equation (48) can then link the initial costate $\boldsymbol{\lambda}_0$ to the final position $\boldsymbol{b}_f$. From the first row of Eq. (48),

$$\delta \boldsymbol{b}_f = \boldsymbol{\Phi}_{12}\delta \boldsymbol{\lambda}_0 = \boldsymbol{\Phi}_{12}\boldsymbol{\lambda}_0 \tag{50}$$

and from Eq. (45),

$$\boldsymbol{\lambda}_0 = \nu 2\boldsymbol{C}^{-1}\boldsymbol{b}_f \tag{51}$$

Hence Eq. (50) is rewritten as

$$\delta \boldsymbol{b}_f = 2\nu \boldsymbol{\Phi}_{12}\boldsymbol{C}^{-1}\boldsymbol{b}_f \tag{52}$$

The nonlinear system in ν and $\boldsymbol{r}_f$ results in

$$\begin{cases} \delta \boldsymbol{b}_f = 2\nu \boldsymbol{\Phi}_{12}\boldsymbol{C}^{-1}\boldsymbol{b}_f \\ d_M^2(\boldsymbol{b}_f) = \bar{d}_M^2 \end{cases} \Rightarrow \begin{cases} \boldsymbol{b}_f - \boldsymbol{b}_p = 2\nu \boldsymbol{\Phi}_{12}\boldsymbol{C}^{-1}\boldsymbol{b}_f \\ \boldsymbol{b}_f^{\top}\boldsymbol{C}^{-1}\boldsymbol{b}_f = \bar{d}_M^2 \end{cases} \tag{53}$$

By rearranging the first equation of Eq. (53),

$$\boldsymbol{b}_f(\mathbb{I}_{2\times 2} - 2\nu \boldsymbol{\Phi}_{12}\boldsymbol{C}^{-1}) = \boldsymbol{b}_p \tag{54}$$

and inserting $\boldsymbol{b}_f$ in the second equation yields

$$\begin{cases} \boldsymbol{b}_f = (\mathbb{I} - 2\nu \boldsymbol{\Phi}_{12}\boldsymbol{C}^{-1})^{-1}\boldsymbol{b}_p \\ [(\mathbb{I} - 2\nu \boldsymbol{\Phi}_{12}\boldsymbol{C}^{-1})^{-1}\boldsymbol{b}_p]^{\top}\boldsymbol{C}^{-1}(\mathbb{I} - 2\nu \boldsymbol{\Phi}_{12}\boldsymbol{C}^{-1})^{-1}\boldsymbol{b}_p = \bar{d}_M^2 \end{cases} \tag{55}$$

Recalling that $\boldsymbol{F} = 2\boldsymbol{\Phi}_{12}\boldsymbol{C}^{-1}$ and defining $\tilde{\boldsymbol{F}} = \det \boldsymbol{F} \cdot \boldsymbol{F}^{-1}$, the second equation of Eq. (55) morphs into a scalar one to be solved for ν:

$$\begin{aligned} \nu^2(\tilde{\boldsymbol{F}}\boldsymbol{b}_p)^{\top}\boldsymbol{C}^{-1}(\tilde{\boldsymbol{F}}\boldsymbol{b}_p) - \nu[\boldsymbol{b}_p^{\top}\boldsymbol{C}^{-1}\tilde{\boldsymbol{F}}\boldsymbol{b}_p + (\tilde{\boldsymbol{F}}\boldsymbol{b}_p)^{\top}\boldsymbol{C}^{-1}\boldsymbol{b}_p] \\ = \bar{d}_M^2 \det{}^2(\mathbb{I} - \nu \boldsymbol{F}) - \boldsymbol{b}_p^{\top}\boldsymbol{C}^{-1}\boldsymbol{b}_p \end{aligned} \tag{56}$$

As for Cartesian case, Eq. (56) has four roots (if all real) corresponding to two local minima and two local maxima of the cost function J. The final B-plane position $\boldsymbol{b}_f$ after CAM execution recovers by evaluating the first equation of Eq. (55) once ν is available. After $\boldsymbol{b}_f$ has been computed, $\boldsymbol{\lambda}_0$ comes directly from Eq. (51):

$$\boldsymbol{\lambda}_0 = \nu 2\boldsymbol{C}^{-1}(\mathbb{I} - 2\nu\boldsymbol{\Phi}_{12}\boldsymbol{C}^{-1})^{-1}\boldsymbol{b}_p \tag{57}$$

Then, the controlled dynamics in Eq. (44) is forwardly integrated to obtain the optimal control profiles.

2. Miss Distance Constraint

The EOCP in B-plane r.f. is here revisited to accommodate a constrained final miss distance. By recalling that the final miss distance in B-plane coordinates is $d = \sqrt{\xi_e^2 + \zeta_e^2} = \|\boldsymbol{b}_f\|$, the nonlinear system in Eq. (53) turns into

$$\begin{cases} \delta\boldsymbol{b}_f = 2\nu\boldsymbol{\Phi}_{12}\boldsymbol{b}_f \\ d(\boldsymbol{b}_f) = \overline{d} \end{cases} \Rightarrow \begin{cases} \boldsymbol{b}_f - \boldsymbol{b}_p = 2\nu\boldsymbol{\Phi}_{12}\boldsymbol{b}_f \\ \|\boldsymbol{b}_f\| = \overline{d} \end{cases} \tag{58}$$

Manipulating the first equation of Eq. (58) to obtain $\boldsymbol{b}_f$ and inserting it into the second equation it yields

$$\begin{cases} \boldsymbol{b}_f = (\mathbb{I}_{2\times2} - 2\nu\boldsymbol{\Phi}_{12})^{-1}\boldsymbol{b}_p \\ \|(\mathbb{I}_{2\times2} - 2\nu\boldsymbol{\Phi}_{12})^{-1}\boldsymbol{b}_p\| = \overline{d} \end{cases} \tag{59}$$

reminding that

$$\left\| \frac{1}{\det(\mathbb{I} - \nu\tilde{\boldsymbol{F}})}(\mathbb{I} - \nu\tilde{\boldsymbol{F}})\boldsymbol{b}_p \right\| = \overline{d}, \quad \text{with } \boldsymbol{F} = 2\boldsymbol{\Phi}_{12} \tag{60}$$

As for the squared Mahalanobis distance case, Eq. (60) is analytically solved for ν and applied to retrieve $\boldsymbol{\lambda}_0$:

$$\boldsymbol{\lambda}_0 = 2\nu(\mathbb{I}_{2\times2} - 2\nu\boldsymbol{\Phi}_{12})^{-1}\boldsymbol{b}_p \tag{61}$$

C. Energy-Optimal CAM Design with Tangential Thrust

In some operational scenarios, the thrust may be required tangential to the trajectory, in other words, parallel to the instantaneous velocity. Consequently, the control acceleration is expressed as a fraction ε of $a_{\max}$, with constrained direction:

$$\boldsymbol{a}_c = a_{\max}\epsilon\boldsymbol{t}, \quad \text{where } \boldsymbol{t} = \frac{\boldsymbol{v}}{v} \tag{62}$$

The performance index is still termed as Eq. (17). The following two sections address the resulting EOCP in ECI and B-plane r.f.

1. ECI Dynamics

The Euler–Lagrange equations are

$$\begin{cases} \dot{\boldsymbol{r}} = \boldsymbol{v} \\ \dot{\boldsymbol{v}} = -\dfrac{\mu}{r^3}\boldsymbol{r} - a_{\max}\left(\boldsymbol{\lambda}_v \cdot \dfrac{\boldsymbol{v}}{v}\right)\dfrac{\boldsymbol{v}}{v} \\ \dot{\boldsymbol{\lambda}}_r = \dfrac{\mu}{r^3}\boldsymbol{\lambda}_v - \dfrac{3\mu\boldsymbol{r}\cdot\boldsymbol{\lambda}_v}{r^5}\boldsymbol{r} \\ \dot{\boldsymbol{\lambda}}_v = -\boldsymbol{\lambda}_r + 2a_{\max}\left(-\left(\dfrac{\boldsymbol{\lambda}_v\cdot\boldsymbol{v}}{v^2}\right)^2\boldsymbol{v} + \dfrac{\boldsymbol{\lambda}_v\cdot\boldsymbol{v}}{v^2}\boldsymbol{\lambda}_v\right) \end{cases}$$

$$BC: \begin{cases} \boldsymbol{r}(t_0) = \boldsymbol{r}_0 \\ \boldsymbol{v}(t_0) = \boldsymbol{v}_0 \\ \boldsymbol{\lambda}_r(t_f) = \nu\dfrac{\partial d_M^2(\boldsymbol{r}_f)}{\partial \boldsymbol{r}_f} = 2\nu\boldsymbol{R}_{2\mathrm{D}}^{\top}\boldsymbol{C}^{-1}\boldsymbol{R}_{2\mathrm{D}}(\boldsymbol{r}_f - \boldsymbol{r}_s) \\ \boldsymbol{\lambda}_v(t_f) = \nu\dfrac{\partial d^2(\boldsymbol{v}_f)}{\partial \boldsymbol{v}_f} = \boldsymbol{0} \\ d_M^2(\boldsymbol{r}_f) - \overline{d}_M^2 = 0 \end{cases} \tag{63}$$

The STM is determined from the state matrix $\boldsymbol{A}$:

$$\boldsymbol{A} = \begin{bmatrix} \boldsymbol{0}_{3\times3} & \mathbb{I}_{3\times3} & \boldsymbol{0}_{3\times3} & \boldsymbol{0}_{3\times3} \\ \boldsymbol{0}_{3\times3} & \boldsymbol{0}_{3\times3} & \boldsymbol{0}_{3\times3} & \boldsymbol{A}_{24} \\ \boldsymbol{0}_{3\times3} & \boldsymbol{0}_{3\times3} & \boldsymbol{0}_{3\times3} & \boldsymbol{0}_{3\times3} \\ \boldsymbol{0}_{3\times3} & \boldsymbol{0}_{3\times3} & -\mathbb{I}_{3\times3} & \boldsymbol{0}_{3\times3} \end{bmatrix},$$
$$\text{with } \boldsymbol{A}_{24} = -a_{\max}\left[\frac{\boldsymbol{v}}{v}\left(\frac{\boldsymbol{v}}{v}\right)^{\top}\right] \tag{64}$$

From this point on, the method is the same as in Sec. III.A.

2. B-Plane Dynamics

The Euler–Lagrange equations in the LVLH frame are

$$\begin{cases} \dot{\boldsymbol{b}} = -a_{\max}\left(\boldsymbol{\lambda}\cdot\boldsymbol{M}\dfrac{\boldsymbol{v}}{v}\right)\boldsymbol{M}\dfrac{\boldsymbol{v}}{v} \\ \dot{\boldsymbol{\lambda}} = \boldsymbol{0}. \end{cases} \quad BC: \begin{cases} \boldsymbol{b}(t_0) = \boldsymbol{b}_0 \\ \boldsymbol{\lambda}(t_f) = \dfrac{\partial d_M^2(\boldsymbol{b}_f)}{\partial \boldsymbol{b}_f} = 2\nu\boldsymbol{C}^{-1}\boldsymbol{b}(t_f) \\ \boldsymbol{b}^{\top}(t_f)\boldsymbol{C}^{-1}\boldsymbol{b}(t_f) - \overline{d}_M^2 = 0 \end{cases} \tag{65}$$

The STM is computed using the matrix $\boldsymbol{A}$:

$$\boldsymbol{A} = \begin{bmatrix} \boldsymbol{0}_{2\times2} & \boldsymbol{A}_{12} \\ \boldsymbol{0}_{2\times2} & \boldsymbol{0}_{2\times2} \end{bmatrix}, \quad \text{with } \boldsymbol{A}_{12} = -a_{\max}\left[\boldsymbol{M}\frac{\boldsymbol{v}}{v}\left(\boldsymbol{M}\frac{\boldsymbol{v}}{v}\right)^{\top}\right] \tag{66}$$

The subsequent derivations are identical to the one reported in Sec. III.B.

D. Fuel-Optimal CAM Design

Despite being analytical, the solution of the EOCP proposed in the previous sections provides a continuous control acceleration profile that can be complex to implement and, because unbounded, may exceed the thrusters' capabilities. In addition, the EOCP does not provide the solution with minimum propellant consumption. All limitations are overcome by solving the fuel-optimal control problem with bounds on the thrust magnitude. The resulting bang-bang control profile is simpler to implement in an operative scenario limiting the propellant consumption. Consequently, this section introduces a numerical procedure to establish a fuel-optimal solution from an energy-optimal one. Effects like the Earth shadowing on power availability and thrusters startup times are left for future investigations.

1. Fuel-Optimal CAM Design in ECI Coordinates

In the FOCP, the cost function is

$$J = \lambda_{v,\mathrm{th}}\int_{t_0}^{t_f} a_{\max}\epsilon\,\mathrm{d}t \tag{67}$$

where $\lambda_{v,\mathrm{th}}$ is a positive scaling factor whose purpose will be clarified afterwards. Thanks to Pontryagin's minimum principle, the optimal control law $(\epsilon^*, \boldsymbol{\alpha}^*)$, providing $\boldsymbol{a}_c = a_{\max}\epsilon^*\boldsymbol{\alpha}^*$, is

$$\begin{cases} \boldsymbol{\alpha}^* = -\dfrac{\boldsymbol{\lambda}_v}{\lambda_v} \\ \epsilon^* = 1 \text{ if } \lambda_v > \lambda_{v,\mathrm{th}} \\ \epsilon^* = 0 \text{ if } \lambda_v < \lambda_{v,\mathrm{th}} \end{cases} \Rightarrow \epsilon = \frac{1}{2}\left[1 - \tanh\left(\frac{\lambda_{v,\mathrm{th}} - \lambda_v}{\rho}\right)\right] \tag{68}$$

This formulation captures the discontinuous bang-bang profile with a hyperbolic tangent function. In Eq. (68), ρ is a scaling parameter that mimics a step function [11,12]. The process equations grow into

$$
\begin{cases}
\dot{\boldsymbol{r}} = \boldsymbol{v} \\
\dot{\boldsymbol{v}} = -\dfrac{\mu}{r^3}\boldsymbol{r} - \dfrac{1}{2}a_{\max}\left[1 - \tanh\left(\dfrac{\lambda_{v,\text{th}} - \lambda_v}{\rho}\right)\right]\dfrac{\boldsymbol{\lambda}_v}{\lambda_v} \\
\dot{\boldsymbol{\lambda}}_r = \dfrac{\mu}{r^3}\boldsymbol{\lambda}_v - \dfrac{3\mu \boldsymbol{r}\cdot\boldsymbol{\lambda}_v}{r^5}\boldsymbol{r} \\
\dot{\boldsymbol{\lambda}}_v = -\boldsymbol{\lambda}_r \\
\dot{\nu} = 0,
\end{cases}
$$

$$
BC: \begin{cases}
\boldsymbol{r}(t_0) = \boldsymbol{r}_0 \\
\boldsymbol{v}(t_0) = \boldsymbol{v}_0 \\
\boldsymbol{\lambda}_r(t_f) = \nu\dfrac{\partial d_M^2(\boldsymbol{r}_f)}{\partial \boldsymbol{r}_f} = 2\nu \boldsymbol{R}_{2\text{D}}^{\top}\boldsymbol{C}^{-1}\boldsymbol{R}_{2\text{D}}(\boldsymbol{r}_f - \boldsymbol{r}_s) \\
\boldsymbol{\lambda}_v(t_f) = \nu\dfrac{\partial d^2(\boldsymbol{v}_f)}{\partial \boldsymbol{v}_f} = \boldsymbol{0} \\
d_M^2(\boldsymbol{r}_f) - \bar{d}_M^2 = 0
\end{cases} \tag{69}
$$

The control acceleration term is, undoubtedly, an approximation of a bang-bang policy. However, this continuous formulation gives comparable results with respect to the optimal bang-bang one when ρ takes sufficiently small values. There is no closed-form solution for this BVP. Yet, the EOCP solution is a suited first guess, and a threshold value for $\lambda_{v,\text{th}}$ is crucial to start the procedure. To this aim, the $\Delta v = \int_{t_0}^{t_f} a_{\max}\lambda_v \, \mathrm{d}t$ of the energy-optimal solution is computed, as well as the equivalent burning time t_b, i.e., the time needed to obtain the same Δv by thrusting with the maximum affordable acceleration:

$$
t_b = \frac{\Delta v}{a_{\max}} = \int_{t_0}^{t_f} \lambda_v \, \mathrm{d}t \tag{70}
$$

The main idea is to define $\lambda_{v,\text{th}}$ so that the thruster fires up for $\lambda_v \geq \lambda_{v,\text{th}}$ (λ_v still belonging to the EOCP) and switched off otherwise. The equivalent bang-bang burning time should be equal to t_b. The procedure to get $\lambda_{v,\text{th}}$ is based on the bisection method:

1) Set two initial boundary values for $\lambda_{v,\text{th}}$ for the first bisection iteration, namely, $\lambda_{v,\text{th}_1} = \max(\lambda_v)$ and $\lambda_{v,\text{th}_2} = \min(\lambda_v)$.

2) Evaluate the burning time t_b^c for $\lambda_v > \lambda_{v,\text{th}_1}$ and for $\lambda_v > \lambda_{v,\text{th}_2}$.

3) Iteratively update λ_{v,th_1} or λ_{v,th_2} with the bisection method taking as cost function $J = t_b^c - t_b$.

4) Do step 3 until $|t_b^c - t_b| \leq \Delta t$ with Δt a prescribed tolerance.

Using the resulting $\lambda_{v,\text{th}}$, and the EOCP states and costates profiles from t_0 to t_f, the TPBVP is solved numerically with the four-stage Lobatto IIIa formula embedded in the *bvp5c* MATLAB function with dynamics of Eq. (69). For the proposed study case (see in Sec. IV.C for more insights), $\rho \simeq 8 \cdot 10^{-6}$ seems a middle ground between the *bvp5c* convergence and the discontinuous profile approximation. Smaller ρ can be achieved by successively solving *bvp5c* using as first guess solution the one obtained for larger ρ. Algorithm 2 summarizes the required steps for CAM design.

2. *Fuel-Optimal CAM Design in B-Plane Coordinates*

Similarly to the ECI case, the discontinuous optimal control laws is substituted by a hyperbolic tangent function and plugged into the dynamics:

$$
\begin{cases}
\dot{\boldsymbol{b}} = -\dfrac{1}{2}a_{\max}\left[1 - \tanh\left(\dfrac{\lambda_{\text{th}} - \|\boldsymbol{M}^{\top}\boldsymbol{\lambda}\|}{\rho}\right)\right]\boldsymbol{M}\boldsymbol{M}^{\top}\dfrac{\boldsymbol{\lambda}}{\lambda} \\
\dot{\boldsymbol{\lambda}} = \boldsymbol{0} \\
\dot{\nu} = 0
\end{cases}
$$

$$
BC: \begin{cases}
\boldsymbol{b}(t_0) = \boldsymbol{b}_0, \\
\boldsymbol{\lambda}(t_f) = 2\nu\boldsymbol{C}^{-1}\boldsymbol{b}(t_f) \\
\boldsymbol{b}^{\top}(t_f)\boldsymbol{C}^{-1}\boldsymbol{b}(t_f) - \bar{d}_M^2 = 0
\end{cases} \tag{71}
$$

Algorithm 2: FOCP-ECI

Input: CDM, $\overline{d_M^2}$ *or* $\overline{P_c}$ $\Delta\theta_{range}$
Output: $\boldsymbol{r}_f, d_M^2, P_c, \boldsymbol{a}_c, \Delta\boldsymbol{v}, \Delta m$
Algorithm:
if $\overline{P_c}$ **then**
  $\overline{d_M^2} = P_c\_2\_squared\_mahalanobis\_distance(\overline{P_c})$
end if
Select a $\Delta\theta$
Start up true anomaly for maneuvering:
$\theta_m = \theta_{\text{TCA}} - \Delta\theta$
T interval of time corresponding to $\Delta\theta$
tspan_backward = [T 0]
tspan_forward =[0 T]
Backward propagation:
Propagate the dynamics backward from θ_{TCA} to θ_m with a pure ballistic motion.
$[\boldsymbol{r}_0, \boldsymbol{v}_0] = keplerian\_propagation([\boldsymbol{r}_{\text{TCA}}, \boldsymbol{v}_{\text{TCA}}]$, tspan_backward, $\mu)$
Compute STM:
Starting from $\boldsymbol{x}_0$, propagate the dynamics with $keplerian\_propagation$ alongside the STM for tspan_forward
Solve the nonlinear system:
Solve [Eq. (34)] for ν and compute $\boldsymbol{\lambda}_{r0}, \boldsymbol{\lambda}_{v0}$ in [Eqs. (35) and (36)]
Controlled forward propagation for the energy-optimal solution:
$[\boldsymbol{R}, \boldsymbol{V}, \boldsymbol{\Lambda}_r, \boldsymbol{\Lambda}_v] = control\_propagation([\boldsymbol{r}_0, \boldsymbol{v}_0, \boldsymbol{\lambda}_{r0}, \boldsymbol{\lambda}_{v0}]$, tspan_forward, $a_{\max}, \mu)$ using Eq. (22) as dynamic model
$\boldsymbol{R}, \boldsymbol{V}, \boldsymbol{\Lambda}_r, \boldsymbol{\Lambda}_v$ are, respectively, n by 3 state and costate matrices; n represents the number of integration steps.
Compute the burning time t_b with Eq. (70) for the energy-optimal case.
Find $\lambda_{v,\text{th}}$ with the bisection method such that the fuel-optimal burning time equates t_b.
Controlled forward propagation for the fuel-optimal maneuver:
The energy-optimal solution is given as a guess to the *bvp5c* solver in MATLAB in terms of state and costate evolution from θ_m to θ_{TCA}.
$[\boldsymbol{R_b}, \boldsymbol{V_b}, \boldsymbol{\Lambda}_{rb}, \boldsymbol{\Lambda}_{vb}, \boldsymbol{m}, v] = bvp5c([\boldsymbol{R}, \boldsymbol{V}, \boldsymbol{\Lambda}_r, \boldsymbol{\Lambda}_v, m_0, v]$ tspan_forward, $a_{\max}, \mu, \lambda_{v,\text{th}})$ adopting the dynamics reported in Eq. (69)
Output computation:
$\boldsymbol{r}_f = \boldsymbol{R_b}(end, :)$
$m_f = \boldsymbol{m}(end)$ final mass
acceleration profile $\boldsymbol{a_c}$ retrieved by plugging $[\boldsymbol{R_b}, \boldsymbol{V_b}, \boldsymbol{\Lambda}_{rb}, \boldsymbol{\Lambda}_{vb}]$ in Eq. (69)
$\Delta\boldsymbol{v}$ is calculated with the integration of $|\boldsymbol{a_c}|$ in time.
$\Delta\boldsymbol{r} = \boldsymbol{r}_f - \boldsymbol{r}_s$
$d_M^2 = squared\_mahalanobis\_distance(\Delta\boldsymbol{r}$, CDM)
$P_c = P_c\_\text{chan}(\Delta\boldsymbol{r}$, CDM)
$\Delta m = m_f - m_0$
$\Delta\boldsymbol{r}$ B-plane projection

The reasoning behind this alternative formulation for $\lambda_{v,\text{th}}$ estimation and TPBVP solution mirrors the ECI procedure.

IV. Results

All the presented techniques are proven on a test case extracted from a large ESA Collision Avoidance Challenge conjunction database [13] (in LEO regime), and made publicly available in [14]. For this contest, ESA has produced 162,634 real CDMs for the competing teams, including 13,154 unique events. These data have been pruned by taking into account conjunctions with $d \leq 2$ km and $P_c > 10^{-6}$, resulting in 2170 conjunctions.

Only one of them is used as test bench in the following sections (see Tables 1 and 2, reporting the state in ECI r.f. and other key

Table 1 Primary and secondary states

State	Value
$\boldsymbol{x}_p$, km	$[2.3305, -1103.7, 7105.9]^{\top}$
$\boldsymbol{x}_s$, km	$[2.3335, -1103.7, 7105.9]^{\top}$
$\boldsymbol{v}_p$, km/s	$[-7.4429, -6.1373\text{e}{-04}, 3.9514\text{e}{-03}]^{\top}$
$\boldsymbol{v}_s$, km/s	$[7.3537, -1.1428, -0.19825]^{\top}$

Table 2 Conjunction parameters

Parameter	Value
P_c	1.3604e−01
d_M^2	0.87166
d, km	0.0432

information of both primary and secondary at CA). Nevertheless, the method has been demonstrated to work with all conjunctions in the set. The objects combined cross-sectional radius $s_A = 29.7$ m, and the primary is assumed to have initial mass $m_0 = 500$ kg, and it features a Hall thruster engine named PPS-1350 G from Safran with an $I_{sp} = 1660$, a nominal thrust $T = 90$ mN, and a power consumption $P = 1500$ W. For full details, check [15], where it reports a catalog of low-thrust engines for small-size satellites.

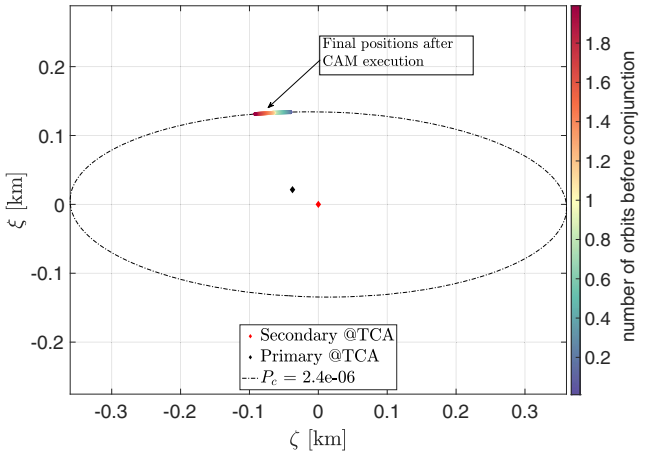

Fig. 2 Final positions in B-plane r.f. after CAM execution obtained for 100 initial maneuvering points from two orbits before TCA to TCA: EOCP with ECI dynamics and constrained squared Mahalanobis distance.

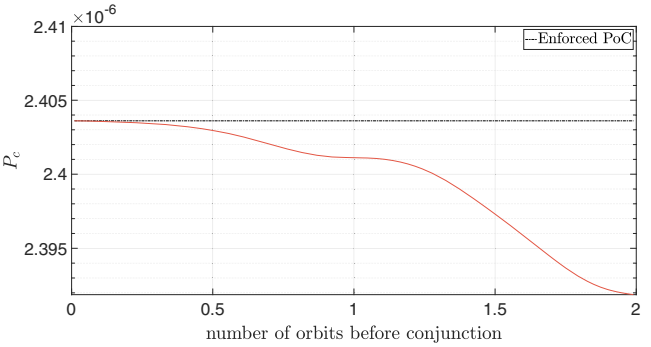

Fig. 3 Final collision probabilities after CAM execution. EOCP with ECI dynamics and constrained squared Mahalanobis distance.

The combined B-plane covariance matrix is

$$\boldsymbol{C} = \begin{bmatrix} 7.21756 & -0.7580 \\ -0.7580 & 51.9201 \end{bmatrix} \cdot 10^{-4} \text{ km}^2 \tag{72}$$

The forthcoming subsections validate the CAM design with a purely Keplerian motion. Although computed with a linearization procedure, all the presented solutions are obtained by propagating the maneuvered trajectories in the nonlinear dynamics starting from the state and costate at t_0. The accuracy is thus quantified by comparing the actual value of P_C against the prescribed one or, equivalently, by showing how well the primary lands on the isoprobability ellipse for different initial maneuvering points.

A. Analytical Solutions

1. *Energy-Optimal Solutions in ECI Coordinates*

For accuracy and robustness assessment of the proposed CAM design problem, 100 equally spaced values of initial maneuvering true anomalies are sampled from two orbits before the TCA till conjunction. The prescribed squared Mahalanobis distance is $d_M^2 = 25$ and the associated collision probability is $P_c = 2.4036 \cdot 10^{-6}$. The method introduced in Sec. III.A applies at each maneuvering point, and the resulting B-plane final positions after CAM execution are plotted in Fig. 2.

The final collision probabilities after CAM execution, i.e., evaluated with $\boldsymbol{r}_f$ from Eq. (29) after the forward propagation of the controlled dynamics, are close to the enforced value (see Fig. 3). The maximum error due to the linearizations is $1.1729 \cdot 10^{-8}$ (two orders of magnitude lower than the imposed P_c), and it decreases when close to conjunction. The final P_c never exceeds the threshold.

The plot in Fig. 4 reports the maximum acceleration commanded during maneuver execution, computed componentwise in the LVLH r.f.. The transverse component prevails for the furthest points from TCA, as already confirmed by Hernando-Ayuso and Bombardelli [5] and Armellin [7], whereas the radial component becomes predominant close to TCA. Each starting maneuvering point features a different time profile of the commanded control acceleration. An example of the resulting control profile is reported in Fig. 5 for a maneuver starting two orbits before TCA.

Finally, Fig. 6a and 6b depict the required maximum thrust and the Δv for every initial firing time. As expected, these two figures of merit dramatically increase for maneuvers starting close to conjunction, eventually making them unfeasible for a low-thrust propulsion system.

As mentioned earlier, Eq. (34) has potentially four solutions, namely, two local maxima and two local minima for the cost function J. These are indicated with stars in Fig. 7 on the ellipse corresponding to the target P_c. Specifically, 300 points are sampled on the ellipse, and the EOCP is solved to reach them at the final time by starting CAM two orbits before TCA. The resulting Δv is computed and plotted in the same figure. As can be seen, the solutions obtained with the proposed analytical CAM design method correspond to the stationary points. Moreover, the two minima are in opposite locations on the ellipse. The corresponding thrust is predominantly tangential or antitangential.

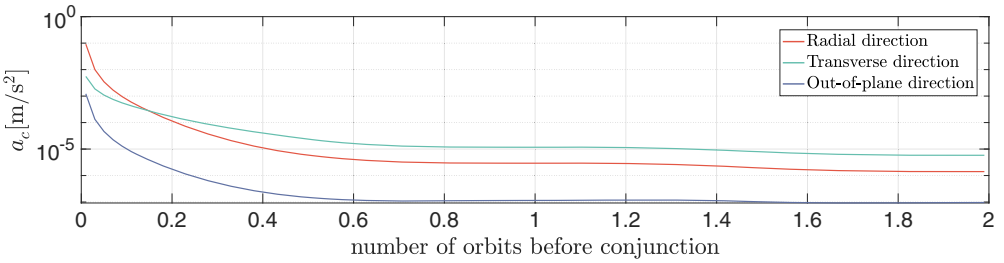

Fig. 4 Equivalent maximum control acceleration a_c for each initial maneuvering point: EOCP with ECI dynamics and constrained squared Mahalanobis distance.

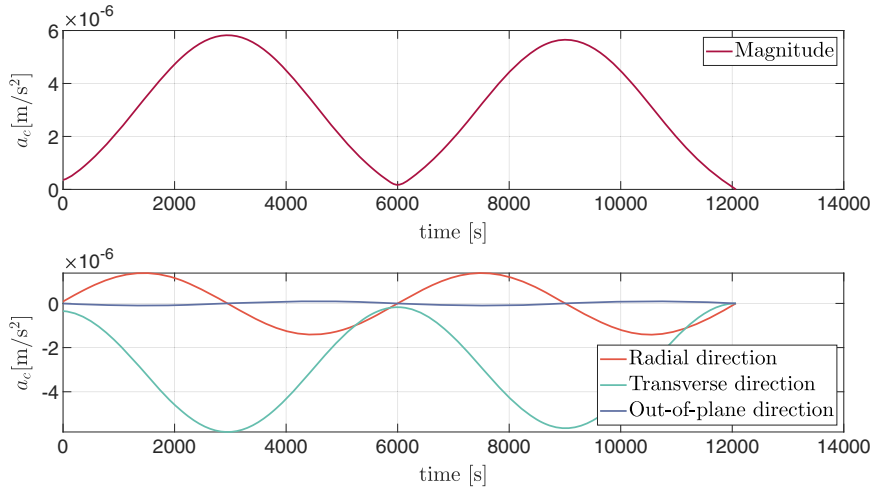

Fig. 5 Control acceleration profile for a maneuver starting two orbits before TCA: EOCP with ECI dynamics and constrained squared Mahalanobis distance.

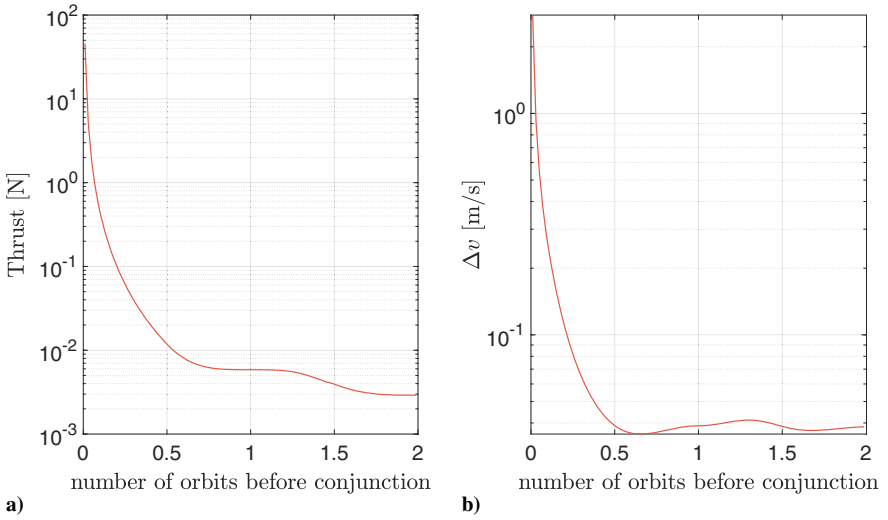

Fig. 6 Maximum thrust (a) and Δv (b) for each initial maneuvering point: EOCP with ECI dynamics and constrained squared Mahalanobis distance.

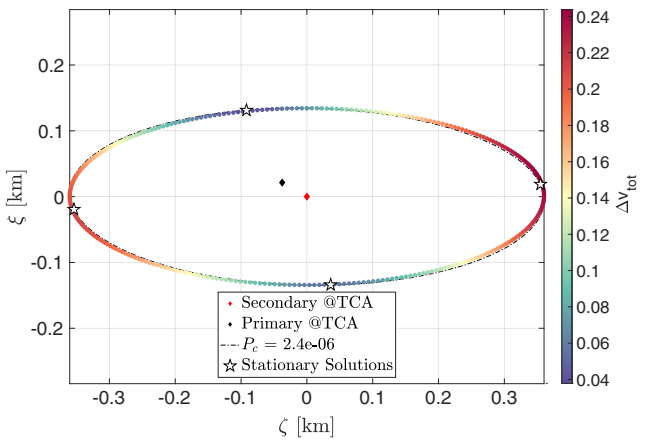

Fig. 7 Equivalent Δv's corresponding to the solutions of the EOCP starting two orbits before TCA reaching 300 points on the target probability ellipse.

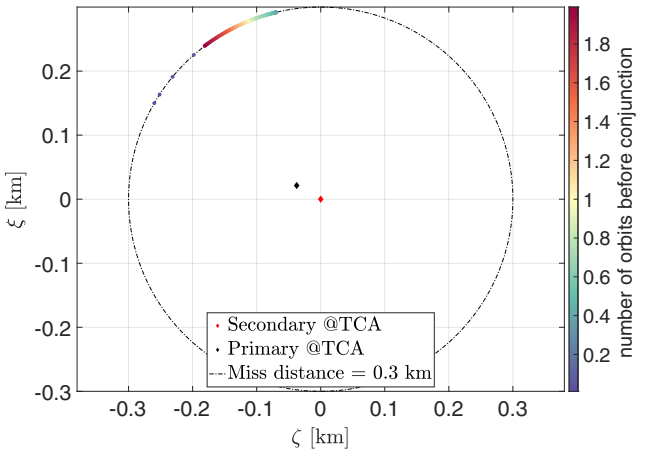

Fig. 8 Final positions in B-plane r.f. after CAM execution, obtained for 100 initial maneuvering points from two orbits before TCA to TCA: EOCP with ECI dynamics and constrained miss distance.

2. Miss Distance Constraint

By adopting the proposed analytical CAM design with the miss distance condition $\overline{d} = 0.3$ km, the final B-plane positions after maneuver execution are reported in Fig. 8. Similarly to the above analysis, 100 equally spaced values of initial maneuvering points have been selected. The error due to linearizations is confined; indeed, the maximum is just $1.1687 \cdot 10^{-4}$ km, three orders of magnitude lower than the enforced miss distance.

3. Energy-Optimal Solutions in B-Plane Coordinates

This section outlines the results of the analytical CAM design method in B-plane dynamics detailed in Sec. III.B. The test case and constraints are the same as Sec. IV.A.1. The commanded CAM yields final positions on the B-plane tight to the isoprobability curve as in Fig. 2.

Valuable insights can be achieved by comparing the trends of the final collision probability after CAM execution. Figure 9 reports a comparison between the final collision probabilities obtained in ECI and B-plane coordinates for each initial maneuvering point. The

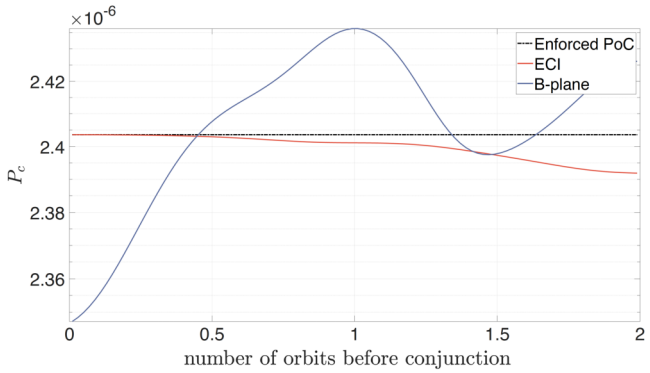

Fig. 9 Final collision probabilities after CAM execution: comparison between the results obtained with the ECI and B-plane formulations. EOCP with constrained squared Mahalanobis distance.

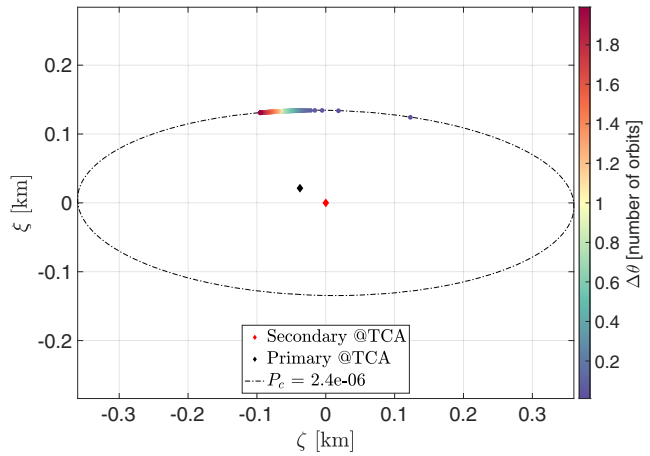

Fig. 10 Final positions in B-plane r.f. after CAM execution obtained for 100 initial maneuvering points from two orbits before TCA to TCA. Tangential EOCP with ECI dynamics and constrained squared Mahalanobis distance.

analytical CAM designed in ECI adheres better to the enforced P_c by never exceeding the corresponding value. Yet, the B-plane formulation provides a maximum error of $5.6354 \cdot 10^{-8}$, featuring the same order of magnitude as the maximum error of the ECI case. The slightly higher approximation error has to do with the circular orbit strong assumption, making the solution less accurate when planning CAMs in highly elliptical orbits as shown in Sec. IV.E.

4. Miss Distance Constraint

The case of constrained final miss distance in B-plane dynamics is addressed hereafter. As noted above, the final positions on the B-plane after maneuver execution are close to those in Fig. 8. Consequently, the corresponding plot is omitted here. The maximum error in ECI dynamics is $1.1687 \cdot 10^{-4}$ km, whereas the B-plane one is $3.3818 \cdot 10^{-4}$ km, roughly three orders of magnitude lower than the applied miss distance value.

B. Energy-Optimal Solutions with Tangential Maneuver

This section delves into the tangential control acceleration case in ECI dynamics with constrained squared Mahalanobis distance. The results of the B-plane formulation and the miss distance terminal condition are unaccounted for because they do not introduce additional insights. For each initial maneuvering point, Fig. 10 represents the final position reached on the B-plane after CAM deployment in the nonlinear dynamics.

The maximum acceleration components commanded for each initial maneuvering point are in the LVLH r.f. The radial component is several orders of magnitude smaller than the transversal one owing to a quasi-primary circular orbit, as seen in Fig. 11.

Figure 12 displays a sample control acceleration over time initiated two orbits before TCA. The profile is in terms of acceleration magnitude (top) and acceleration components in the LVLH r.f. (bottom). The commanded acceleration is close to transversal, expected for a tangential maneuver initiated well in advance. For each initial point, Fig. 13b if compared to Fig. 6a exhibits a higher Δv and a maximum thrust level (see Fig. 13a) near conjunction by virtue of a fixed firing direction.

Figure 14 compares the actual P_c obtained by the tangential maneuver formulated in ECI with its prescribed value. The maximum error is $4.9582 \cdot 10^{-8}$, two orders of magnitude less than the target P_c.

C. Fuel-Optimal Solutions

The transformation to a fuel-optimal solution is validated in this section by testing the algorithm on 15 equally spaced initial maneuvering points from 0.7 to 2 orbits before TCA. Results may significantly vary with higher or lower values of maximum allowable thrust acceleration $a_{\max}$ and tuning parameter ρ. For the case at hand, $\rho = 8 \cdot 10^{-6}$ and $a_{\max} = 1.8 \cdot 10^{-4}$ m/s^2 is found from

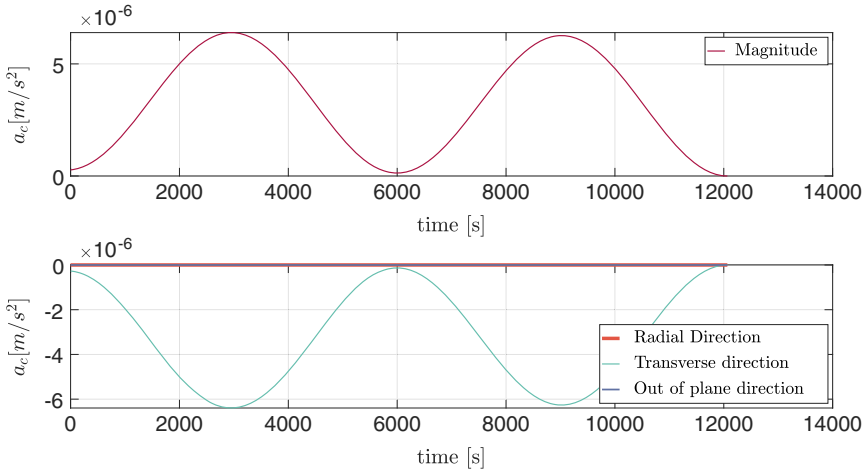

Fig. 11 Maximum control acceleration a_c for each initial maneuvering point: tangential EOCP with ECI dynamics and constrained squared Mahalanobis distance.

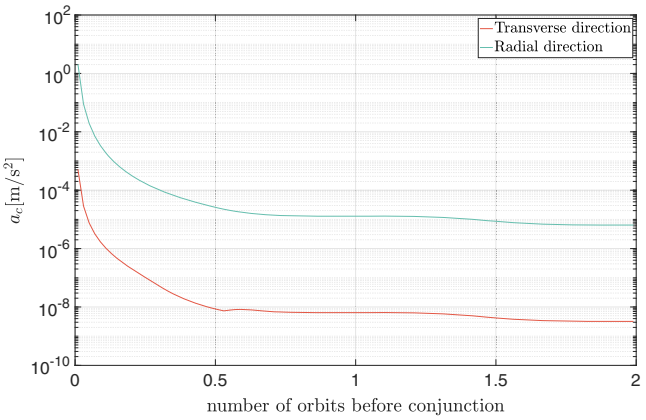

Fig. 12 Control acceleration profile for a maneuver starting two orbits before TCA. Tangential EOCP with ECI dynamics and constrained SMD.

$$a_{\max} = \frac{T}{m_0} \tag{73}$$

where m_0 is the initial mass, and T is the nominal thrust level. For the chosen parameters, 0.7 orbits before the conjunction is the lower bound in terms of initial maneuvering point for the algorithm's convergence. A higher ρ may negatively affect the target collision probability when plugging the obtained costates into a discontinuous control profile. Figure 15 accounts for the final positions reached on the B-plane with a fuel-optimal thrusting profile obtained through the *bvp5c* solver. To help the solver convergence, the jacobians for both dynamics and boundary conditions are provided. Further information is available at [16].

Figure 16 displays the collision probability evolution for different initial maneuvering points. Three cases are analyzed:

1) FOCP-SFD (smooth finite difference) in green is the collision probability yielded by a smoothing approach, described in Eq. (69).

2) FOCP-DFD (discontinuous finite difference) in yellow stands for the collision probability computed with the FOCP-SFD initial costates and inputted in a discontinuous thrust profile:

$$\boldsymbol{a}_c = -\frac{1}{2}(\lambda_v >= \lambda_{\text{th}}) a_{\max} v \lambda v \tag{74}$$

3) Finally, FOCP-DSS (discontinuous simple shooting) in red refines the initial conditions of FOCP-SFD with a discontinuous thrust profile [see Eq. (74)], i.e., by a simple shooting approach).

FOCP-SFD and FOCP-DSS meet the constraint on P_c at a precision dictated by the solver convergence tolerance. FOCP-DFD instead slightly deviates from the reference P_c as the control profile used for the validation (discontinuous) is different from the one used

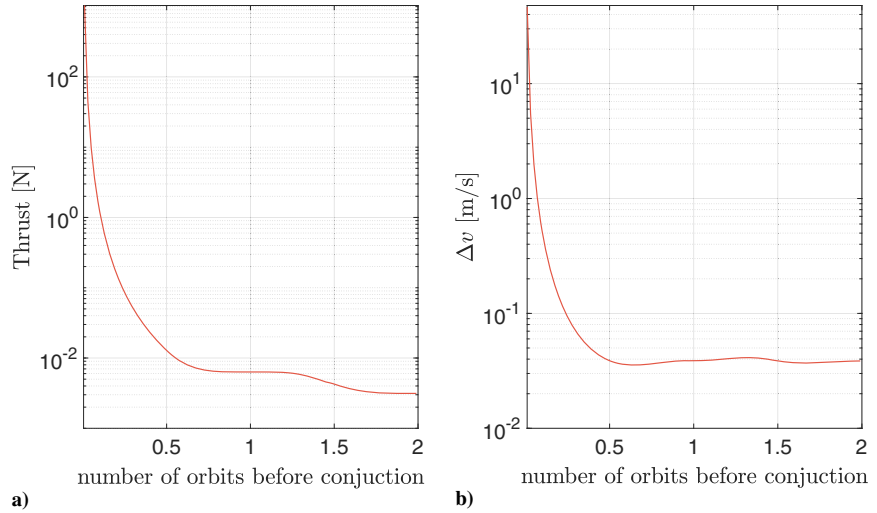

Fig. 13 Maximum thrust (a) and Δv (b) for each initial maneuvering point: tangential EOCP with ECI dynamics and constrained squared Mahalanobis distance.

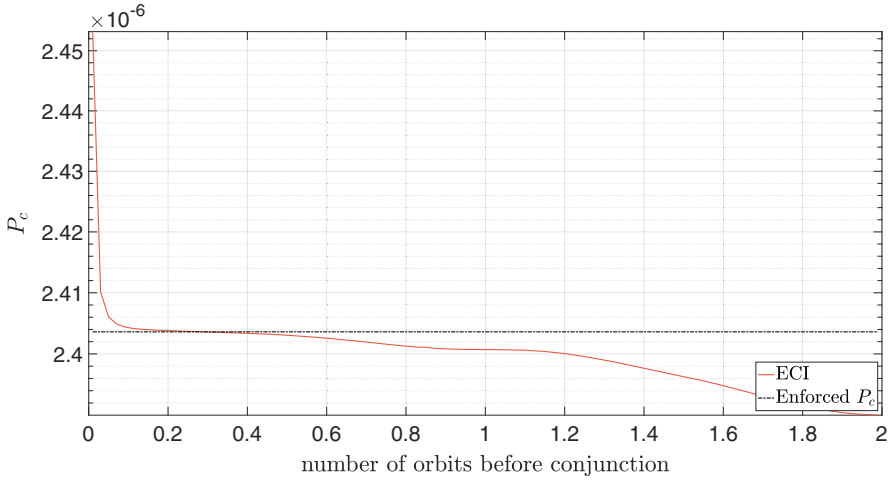

Fig. 14 Collision probability profile after the dynamics propagation: tangential EOCP in ECI coordinates and constrained squared Mahalanobis distance.

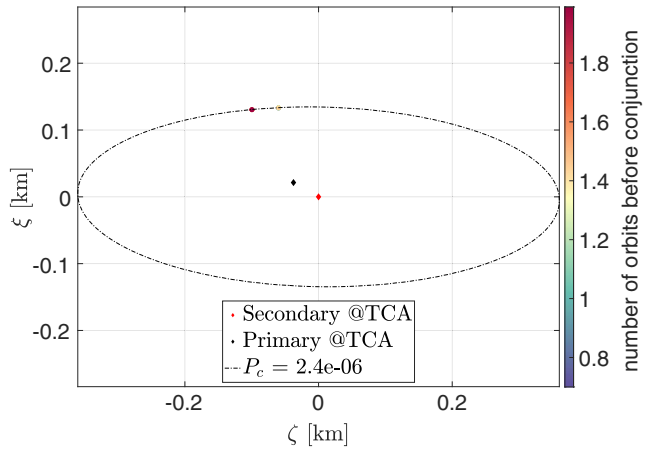

Fig. 15 Final position in B-plane r.f. reached after the fuel-optimal maneuver performed from 0.7 to 2 orbits before TCA.

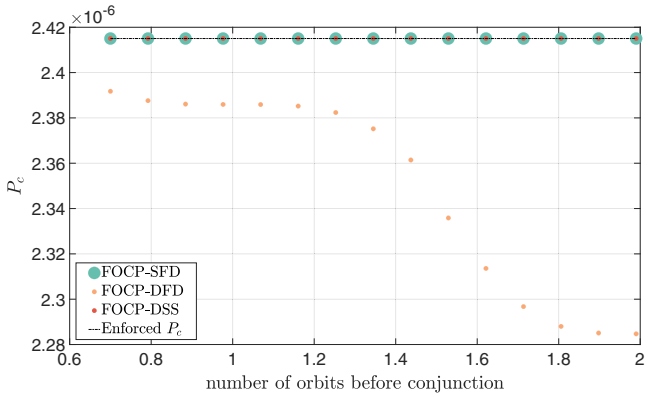

Fig. 16 Collision probability profile after the dynamics propagation: FOCP in ECI coordinates and constrained squared Mahalanobis distance for 15 initial maneuvering points.

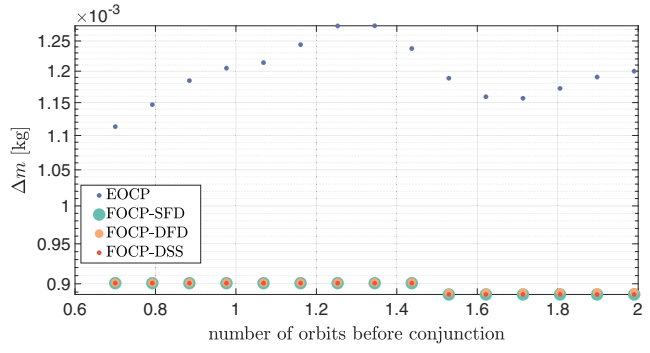

Fig. 17 Comparison between the fuel mass consumption of the EOCP and FOCP obtained for 15 initial maneuvering points from 0.7 to 2 orbits before TCA.

to compute the initial costates (continuous). Nevertheless, the overall error is still acceptable because P_c is associated with a position error of decimeters in B-plane coordinates. As expected, the offset increases with early maneuver planning. Actually, the overall firing time of FOCP-SFD shrinks, causing a higher relative Δv error for discontinuous profiles. Note that in all the cases the linearization errors are absent as the problem is solved directly in the nonlinear dynamics.

Pertaining to fuel consumption, Fig. 17 follows the same nomenclature of Fig. 16. The EOCP solution always requires a higher propellant mass when compared to FOCP-SFD, FOCP-DFD, and FOCP-DSS. Notably, the three different fuel-optimal formulations

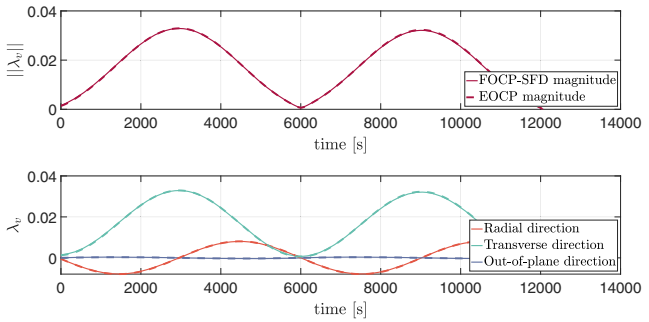

Fig. 18 Velocity costate (λ_v) profile for the energy-optimal CAM (dashed lines) and the fuel-optimal control (solid lines) initiated two orbits before TCA for the FOCP-SFD case.

do not differ at all. On average, a fuel-optimal solution allows between $2.1 \cdot 10^{-4}$ and $3.6 \cdot 10^{-4}$ kg of propellant mass savings for the proposed CAM scenario. Figures 16 and 17 finally prove that if ρ is small enough, FOCP-DFD is a viable solution for a discontinuous thrust while fulfilling all boundary constraints.

Moving on to the costate time evolution, Fig. 18, the EOCP profile seems to almost overlap the FOCP-SFD one, demonstrating that the energy-optimal solution is a fair initial guess. Figures 18–20 show the acceleration profiles for the FOCP-SFD and FOCP-SFD cases, respectively. It is clear that, with a sufficiently low ρ, the former tends to mimic the discontinuous behavior of the control profile. As for the analytic solution, the transverse component of the acceleration vector prevails for CAMs initiated far from conjunction.

D. Perturbations Effect

The performance of the proposed analytical energy-optimal solution is now tested in more refined orbital dynamics, including the effects of the first 10 Earth's gravitational harmonics and drag (with coefficient $c_D = 2.2$ and area-to-mass ratio equal to 0.3), which are predominant in the LEO regime. More specifically, the analytical solution of Sec. III.A provides the control acceleration profiles then comprised in the perturbed dynamics.

The final positions reached on the B-plane after CAM execution in the perturbed nonlinear dynamics are plotted in Fig. 21.

The collision probability after CAM execution is investigated in Fig. 22 for the perturbed and the unperturbed dynamics. As intended, the former differs more from the established P_c (with a maximum deviation of $1.0531 \cdot 10^{-7}$ compared to $1.1729 \cdot 10^{-8}$ of the Keplerian case). Yet, the designed CAM can be considered to be effective and safe. Similar considerations hold for the fuel-optimal case, shown in Fig. 23.

E. Highly Elliptical Orbits

In this section, differently from [5], we show the applicability of our methods to eccentric primary and secondary orbits. Their orbital data are in Table 3 at the conjunction (artificially generated). The primary trajectory has an eccentricity $e_p = 0.1235$ and the secondary has $e_s = 7.0298 \cdot 10^{-2}$; the conjunction data are given in Table 4. The EOCP is planned for both ECI and B-plane coordinates as shown in Figs. 24a and 24b. The first formulation is not affected by the eccentricity; indeed, all terminal points accurately land on the isoprobability curve. For the B-plane dynamics, the dots displayed in Fig. 24b slightly divert from the imposed collision probability curve. As asserted by [5], the main assumption of the B-plane formulation is circular orbit motion.

The combined B-plane covariance matrix is

$$\boldsymbol{C} = \begin{bmatrix} 20.7503 & -9.2100 \\ -11.21 & 464.7503 \end{bmatrix} \cdot 10^{-3} \text{ km}^2 \qquad (75)$$

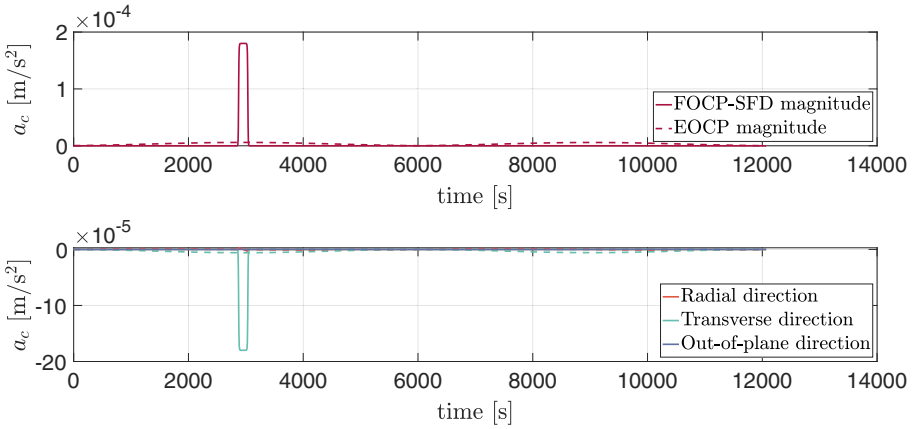

Fig. 19 Control acceleration time profile for the EOCP CAM (dashed lines) and for FOCP-SFD (solid lines) initiated two orbits before the TCA, $\rho = 8 \cdot 10^{-6}$.

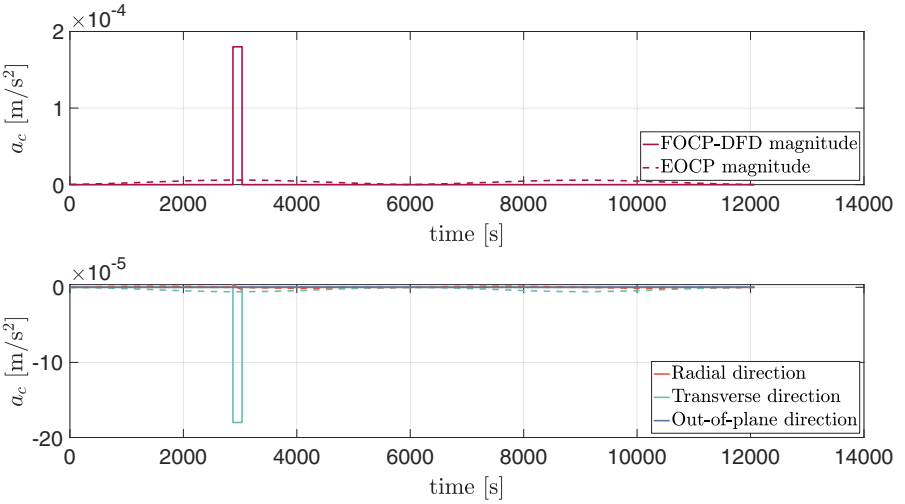

Fig. 20 Control acceleration time profile for the energy-optimal CAM (dashed lines) and the fuel-optimal control (solid lines) in case of a maneuver initiated two orbits before conjunction: FOCP-DFD case.

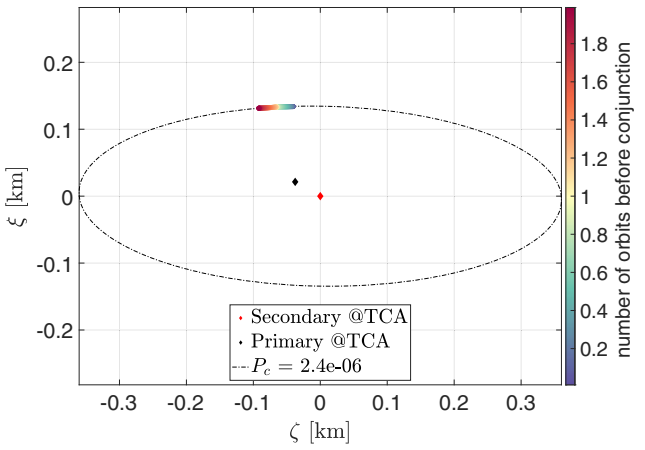

Fig. 21 Final positions in B-plane r.f. after EOCP CAM execution in perturbed dynamics.

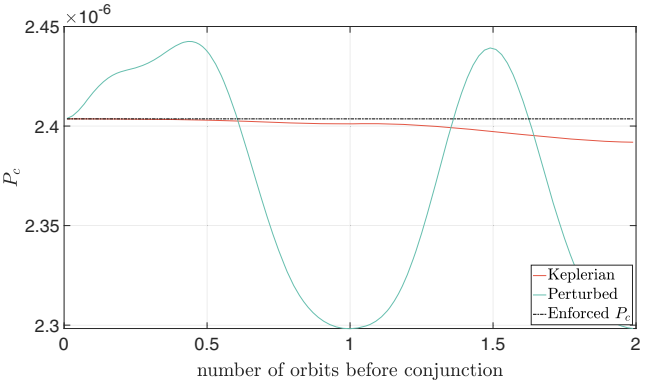

Fig. 22 Collision probability profile after dynamics propagation: comparison between unperturbed and perturbed dynamics. EOCP in ECI coordinates with constrained SMD.

F. Computational Time

In this section, we assess the EOCP and FOCP algorithms' performance in terms of computational time. The algorithms have been developed with the Rosetta emulated MATLAB® 2020a version and executed on an Apple M1 Chip with an 8-Core CPU and 16 Gb of RAM. Since the processing time is fractions of a second, a statistical analysis simulates 100 unique events selected from the ESA Collision avoidance database and averaging the resulting computational times.

Notably, Fig. 25 reports the average computational times obtained from two up to eight orbits before TCA. These, in turn, are split into several contributions: the STM integration (in green), the analytical derivation of the initial costate (in red), and the forward propagation to retrieve the control acceleration to be commanded (in yellow). As expected, the STM and the forward propagation times decrease close

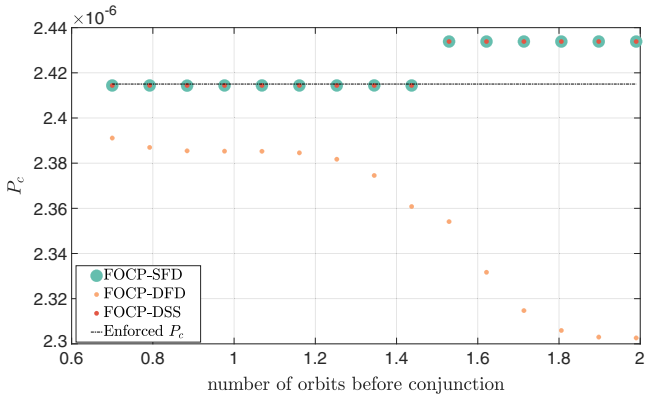

Fig. 23 Collision probability profile after dynamics propagation: comparison among FOCP-SFD, FOCP-DFD, and FOCP-DSS.

Table 3 Conjunction parameters

Parameter	Value
P_c	2.7023e−03
d_M^2	2.0574e−05
d, km	1.08231e−02

Table 4 Primary and secondary states

State	Value
$\boldsymbol{x}_p$, km	$[8500, -100, 200]^\top$
$\boldsymbol{x}_s$, km	$[8500.01, 99.995, 199.97]^\top$
$\boldsymbol{v}_p$, km/s	$[0.1, 7.2479, 0]^\top$
$\boldsymbol{v}_s$, km/s	$[-0.1, 7.0479, 0.7]^\top$

to TCA. Yet, the overall computational time is always of the order of 10^{-1} s in the current MATLAB implementation, and it looks promising for a prospective on-board implementation. Turning on to the FOCP, in Fig. 26 the simulation spans only from 0.7 to 2 orbits to ensure the algorithm convergence when setting a fixed $a_{\max}$ for all iterations. Due to the additional *bvp5c* numerical solver overhead (in green), a CAM design takes from 10 to 20 times more than the corresponding EOCP one; nevertheless, it is relatively fast, being the overall CPU run time always less than 4 s.

V. Conclusions

We have derived purely analytic formulations for energy-optimal low-thrust CAMs for short-term encounters with constant and uncorrelated covariances and spherical object approximation in ECI and

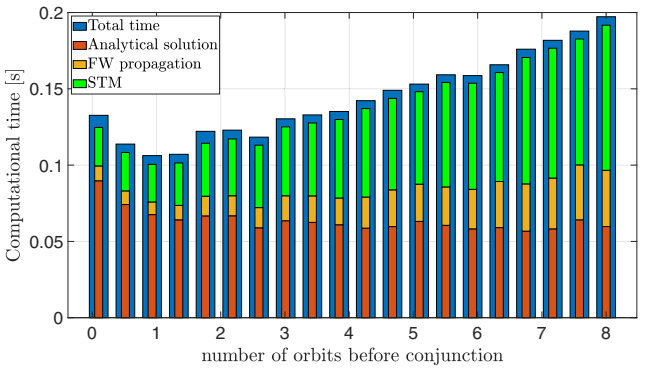

Fig. 25 Average EOCP computational times for up to eight orbits before TCA, divided in the their main contributions.

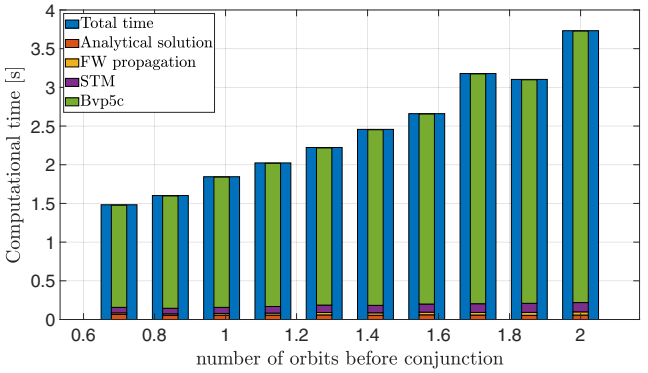

Fig. 26 Average FOCP-SFD computational times obtained up to two orbits before TCA, divided in the their main contributions.

B-plane reference frames. Starting from different initial maneuvering points, the algorithm enforces final conditions in terms of collision probability, squared Mahalanobis distance, and miss distance. On average, the energy-optimal control problem (EOCP) in the B-plane coordinates turns out to be less accurate than the ECI one due to its first-order dynamics approximation. In addition, optimal CAMs, following other similar works on the same topic, tend to be close to tangential if planned in advance. In some operational scenarios, it can be preferable to command a merely tangential thrust sacrificing only a little in optimality. Lastly, a method leveraging the EOCP solution solves the FOCP with bounds on the control acceleration for propellant mass savings.

The algorithms were tested on realistic short-term encounters in low Earth orbit. We have shown that the employed linearizations have little effect on the constraints violations and that Keplerian dynamics are appropriate for maneuver planning, even for highly elliptical orbits. The limited computational time and the robustness of the algorithms make them a promising approach for onboard CAM design.

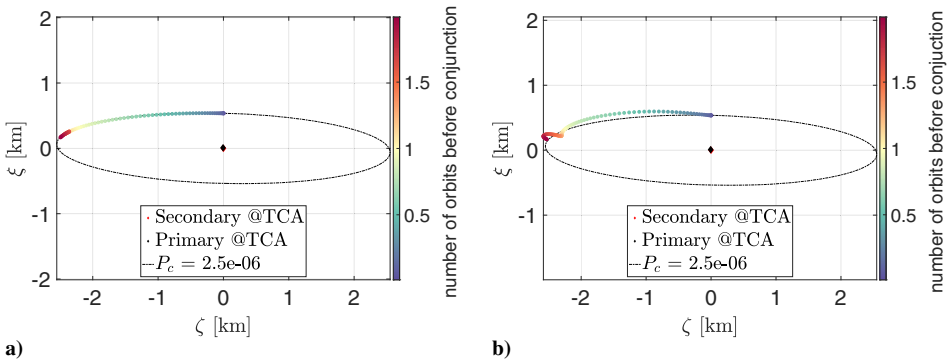

Fig. 24 Final spacecraft position with a CAM planned in ECI coordinates (a) and in B-plane ones (b) for highly elliptical primary and secondary orbits.

References

[1] Reiter, J., and Spencer, D., "Solutions to Rapid Collision-Avoidance Maneuvers Constrained by Mission Performance Requirements," *Journal of Spacecraft and Rockets*, Vol. 55, No. 4, 2018, pp. 1040–1048. https://doi.org/10.2514/1.A33898

[2] Salemme, G., Armellin, R., and Di Lizia, P., "Continuous-Thrust Collision Avoidance Manoeuvres Optimization," AIAA Paper 2020-0231, 2020. https://doi.org/10.2514/6.2020-0231

[3] Schiavo, A., "Numerically Efficient Design of Low-Thrust Collision Avoidance Manoeuvre," Master's Thesis, School of Industrial and Information Engineering, Dept. of Aerospace Science and Technology, Politecnico di Milano, Milan, 2020.

[4] Gonzalo, J., Colombo, C., and Di Lizia, P., "A Semi-Analytical Approach to Low-Thrust Collision Avoidance Manoeuvre Design," *70th International Astronautical Congress (IAC 2019)*, Paper IAC-19,A6,2,3,x53663, 2019, pp. 1–9.

[5] Hernando-Ayuso, J., and Bombardelli, C., "Low-Thrust Collision Avoidance in Circular Orbits," *Journal of Guidance, Control, and Dynamics*, Vol. 44, No. 5, May 2021, pp. 983–995. https://doi.org/10.2514/1.G005547

[6] Belmonte Hernandez, C., Martínez Chamarro, A., and Armellin, R., "Low-Thrust Collision Avoidance Maneuvers Using Optimal Control Theory and Convex Optimization," *31st Space Flight Mechanics Meeting*, Vol. 41, No. 31, 2021, pp. 2470–2475.

[7] Armellin, R., "Collision Avoidance Maneuver Optimization with a Multiple-Impulse Convex Formulation," *Acta Astronautica*, Vol. 186, 2021, pp. 347–362. https://doi.org/10.1016/j.actaastro.2021.05.046

[8] Chan, F., Spacecraft Collision Probability, Aerospace Press, Reston, VA, 2008, Chaps. 3 and 4, pp. 63–83, https://books.google.it/books?id=c-ceAQAAIAAJ.

[9] Valsecchi, G. B., Milani, A., Gronchi, G. F., and Chesley, S. R., "Resonant Returns to Close Approaches: Analytical Theory," *Astronomy and Astrophysics*, Vol. 408, No. 3, 2003, pp. 1179–1196. https://doi.org/10.1051/0004-6361:20031039

[10] Bryson, A., *Applied Optimal Control: Optimization, Estimation and Control*, Halsted Press Book, Taylor & Francis, London, 1975, pp. 47–55, https://books.google.it/books?id=P4TKxn7qW5kC.

[11] Rasotto, M., Armellin, R., and Lizia, P. D., "Multi-Step Optimization Strategy For Fuel-Optimal Orbital Transfer of Low-Thrust Spacecraft," *Engineering Optimization*, Vol. 48, No. 3, 2016, pp. 519–542. https://doi.org/10.1080/0305215X.2015.1025773

[12] Taheri, E., and Junkins, J. L., "Generic Smoothing for Optimal Bang-Off-Bang Spacecraft Maneuvers," *Journal of Guidance, Control, and Dynamics*, Vol. 41, No. 11, 2018, pp. 1–6. https://doi.org/10.2514/1.G003604

[13] "Collision Avoidance Challenge," ESA, https://kelvins.esa.int/collision-avoidance-challenge/data/ [retrieved 2 March 2021].

[14] Roberto, A., "Conjunction," https://github.com/arma1978/conjunction/ [retrieved 2 March 2021].

[15] O'Reilly, D., Herdrich, G., and Kavanagh, D., "Electric Propulsion Methods for Small Satellites: A Review," *Aerospace*, Vol. 8, Jan. 2021, p. 22. https://doi.org/10.3390/aerospace8010022

[16] "bvpset," Mathworks, https://www.mathworks.com/help/matlab/ref/bvpset.html [retrieved 25 April 2022].